ELSEVIER

Contents lists available at ScienceDirect

# International Journal of Heat and Mass Transfer

journal homepage: www.elsevier.com/locate/hmt



# Discrete Green's functions and spectral graph theory for computationally efficient thermal modeling



Kevin D. Cole a,b,\*, Alex Riensche a,b, Prahalada K. Rao a,b

- <sup>a</sup> Mechanical and Materials Engineering Department
- b University of Nebraska-Lincoln, W342 Nebraska Hall, P.O. Box 880526, Lincoln, NE 68588-0526, United States

#### ARTICLE INFO

Article history:
Received 11 August 2021
Revised 6 October 2021
Accepted 15 October 2021
Available online 24 November 2021

Keywords:
Heat conduction
Additive manufacturing
Thermal modeling
Spectral graph method
Greens\_function
Semi-analytical method

#### ABSTRACT

This work concerns solutions of the heat equation with the spectral graph method, for which the temperature is defined at discrete points in the domain and the spatial relationship among the points is described by a graph. The heat equation on the graph is solved using matrix techniques involving the eigenvectors and eigenvalues of the Laplacian matrix. The spectral graph approach precludes the computationally intensive meshing and numerous time-integration steps of the finite element method. In the present work, the spectral graph method is extended to include heat loss at the boundaries with a generalized boundary condition, and physics-based edge weights are introduced which simplify the calibration process. From this approach a discrete Green's function is defined which allows for solutions under a variety of heating conditions including: space-varying initial conditions; time-and-space varying internal heating; and, time-and-space-varying heating at boundaries of type 1 (Dirichlet), type 2 (Neumann) and type 3 (Robin). Results are provided for benchmark heat transfer problems in one spatial dimension and in three spatial dimensions, and verification is provided by comparison with exact analytical solutions and finite difference solutions. The spectral graph method converges within 0.4% error of the analytical solution. The practical utility of the approach is demonstrated by thermal simulation of a multilayer additive manufacturing process. The spectral graph results are compared to experimentally-obtained temperature data for two metal parts, with error less than 5% of the experimental measurements, with computation time less than one minute on a desktop computer.

© 2021 Elsevier Ltd. All rights reserved.

#### 1. Introduction

In the spectral graph method the heat equation is solved over a discrete set of nodes. The novelty of the present work is that the spectral graph method is combined with discrete Green's functions through treatment of a generalized boundary condition.

The strength of the spectral graph (SG) method lies in the ease with which any geometry may be represented by a collection of nodes dispersed throughout the body. Previous work by the authors has shown that the SG method may be computed faster than commercial finite element codes for comparable precision, for thermal simulation of additive manufacturing [1–5]. That previous work involved insulated boundaries, with boundary heat loss included as an adjustment to the boundary temperatures, external to the SG method.

The strength of the Green's function (GF) method is that several types of heating conditions may be addressed with straightforward

\* Corresponding author.

E-mail address: kcole1@unl.edu (K.D. Cole).

steps if the GF is known. Discrete building-block solutions can be constructed from the GF to treat heating conditions that vary over space and over time [6]. However finding the GF is a central challenge [7, p. 101].

In the present work, the geometric universality and computational speed of the SG method is combined with the multiple-heating capability and mathematical rigor of the GF method. The improved method can treat boundary conditions of type 1, 2, and 3, under a variety of heat-addition conditions, and has great potential to provide rapid thermal simulations of a variety of industrial processes.

# 1.1. Literature review

The pertinent literature will be reviewed in the areas of the spectral graph method, discrete Green's functions, and thermal simulation of additive manufacturing.

# 1.1.1. Spectral graph method

Recently the spectral graph (SG) method has been used to solve the heat conduction equation in the context of image processing and filtering of other large data sets [8–10]. In a study of image smoothing, Zhang and Hancock use randomly assigned node locations to construct a discrete Laplacian matrix and subsequently to solve the heat conduction equation [10]. A review paper by Solomon [11] shows that the Laplacian matrix constructed from a uniformly spaced grid gives a solution to the heat conduction equation. However, if the grid is not equally spaced, the relationship to the correct solution of the heat conduction equation is not clear.

#### 1.1.2. Discrete Green's function

Several authors have developed a discrete Green's function (GF) for steady diffusion. Bendito et al. [12] give a procedure for finding the steady discrete GF using graph theory for Dirichlet (type 1) boundary conditions for application to electric resistor networks. Zhang et al. [8] discuss discrete GF for diffusion in large data graphs for a social network application, and an approximate matrix inversion technique is used to obtain a few eigenvalues from very large Laplacian matrices. Gilbert et al. [13] develop discrete GF with boundary conditions of type 1, 2 or 3 with application to scattering of light, with examples provided in one and two dimensions. Arauz et al. [14] discuss procedures for finding the discrete GF from graph theory by studying subnetworks, to mitigate the computational burden when the Laplacian matrix is very large. Tewary and Garboczi [15] find the discrete GF for a two dimensional composite body using a semi-analytic Fourier integral method applied to steady heat transfer and electrostatic potential.

There has been some work on a discrete GF for transient diffusion using graph theory. Chung et al. [16] introduce a discrete form of Green's theorem on graphs and give an example of diffusion driven by non-homogeneous Dirichlet (type 1) boundary. However no numerical results are provided. Xu et al. [17] studied random walks on graphs and defined a discrete GF for Neumann (type 2) boundary conditions. Time evolution of the solution is replaced by a focus on the number of steps in a random walk for transport from one point to another on the graph.

There are many applications of the finite element method for discrete GF applied to the heat equation. Mansur et al. have a series of papers based on the finite element method: one paper introduces the method for the heat equation and provides examples in two spatial dimensions [18]; another paper provides details of the time integration of the discrete GF to control numerical stability [19]; and, another defines the discrete GF in the Laplace domain with a Laplace-inversion integral in place of a time integral [20]. Zhang and Li [21] use the discrete GF for two-dimensional heat transfer in soil surrounding subway tunnels. Sodan et al. [22] use time convolution to apply discrete GF to thermal effects in galliumnitride electronic devices.

Several authors have worked with discrete GF constructed by other means. Melnikov and Reshniak [23] incorporated analytical GF which satisfied some of the boundary conditions into a boundary integral formulation in order to numerically satisfy all of the boundary conditions; examples in two spatial dimensions were provided. Mai et al. [24] developed the GF for a finite two-dimensional domain by distributing fundamental solutions along the boundary, which may be type 1, 2 or 3. Wang et al. [25] used an integral-transform technique to find the GF for non-Fourier heat conduction in unbounded domains, with application to microscale heat transfer. Eaton [26] built a discrete GF from analytical boundary layer solutions for convection heat transfer.

# 1.1.3. Thermal simulation of additive manufacturing

The impact of thermal effects on defects in additive manufacturing is well documented [27–31]. Through the use of thermal simulation, it is possible to minimize the occurrence of defects, such as geometric deformation and microstructure heterogeneity,

by predicting the effect of process conditions and part design on the temperature history in the build, without relying on extensive build-and-repeat empirical optimization [32].

Accurate quantitative modeling approaches based on finite element (FE) analyses have been successfully developed and applied for understanding the thermal aspects of AM at the part-level, as summarized in several references [33–37]. However, these pioneering non-proprietary approaches are computationally expensive, with simulation of a few deposited layers amounting to many hours, if not days [38,39]. For example, Cheng et al. reported that the computation time for thermomechanical analysis for a 6 mm cuboid shape part exceeds 92 hours [38].

Hence, newer efficient approaches are needed to predict the temperature distribution under different part designs and with various process parameters; this is the motivation for the present work. In the context of FE-based modeling there exist several commercial, proprietary approaches, such as Autodesk Netfabb and Ansys 3DSim, that have leveraged adaptive meshing principles to drastically reduce the computational time. However, the underlying mathematics of these commercial software applications is proprietary [36,40]. Furthermore, there is a large variation in the results among proprietary software, as large as 80% in a recent benchmarking study [41].

#### 1.2. Organization of the paper

In the remainder of the paper, Section 2 provides a development of the Green's function approach, with the discrete GF constructed from the spectral graph method based on nodal energy balances on an unstructured grid. Section 3 contains examples of the method applied to geometries with planar boundaries under two different heating conditions, with verification provided by comparison with exact analytical solutions and finite difference solutions in one spatial dimension and with exact analytical solutions in three spatial dimensions. Section 4 demonstrates the method for thermal simulation of a multilayer additive manufacturing process on bodies with severe overhang, and the results are validated by comparison with experimental temperature values. Section 5 contains a summary and discussion of the work.

# 2. Theory and development

The discrete Green's function (GF) is a matrix of size  $(n \times n)$ , where n is the number of nodes in the body. Each row of the GF matrix contains the temperature response in the body caused by an impulse of heat at one node. All the rows of the GF matrix together provide the overall response to heating at any of the nodes in the body.

In this section the discrete GF method is introduced in several steps. Section 2.1 provides the overall relation between temperature and the discrete GF for several heating conditions, which we call the discrete GF solution equation. In Section 2.2 the discrete GF is constructed from the spectral graph method which involves the Laplacian matrix of a graph. Section 2.3 provides details of the Laplacian matrix by examining an energy balance on each node in the body. Section 2.4 shows how the distribution of nodes in the body affects the edge weights used to connect nodes to one another. Section 2.5 demonstrates that although the discrete GF is discrete in space, it is analytic in time. Section 2.6 provides an overview of the method and its limitations.

# 2.1. Discrete Green's function solution equation

In the continuous Green's function (GF) method, the boundary value problem for temperature is recast into an integral expression containing the GF multiplied by each of the heating effects present in the problem, such as the initial condition, the internal heating function, and any boundary heating functions [7, chap. 3]. This GF solution equation is flexible and powerful because one GF allows for a large family of solutions to be treated in a straightforward manner. In this section, the discrete GF solution equation is presented by analogy with the continuous GF method. The starting point is the boundary value problem for temperature:

$$\frac{1}{\alpha} \frac{\partial T}{\partial t} = \nabla^2 T + \frac{1}{k} g(\mathbf{r}, t) \quad \text{(domain R)}$$

$$k\frac{\partial T}{\partial n_m} + h_m T = h_m T_{\infty m} + q_m \qquad (m^{th} \text{ boundary of R})$$
 (2)

$$T(\mathbf{r}, t = 0) = T_0(\mathbf{r})$$
 (initial condition) (3)

Material properties are conductivity k [ $Wm^{-1}K^{-1}$ ] and diffusivity  $\alpha$  [ $m^2s^{-1}$ ]. Here  $n_m$  represents the outward normal vector on the  $m^{th}$  portion of the body surface, each of which is characterized by convection coefficient  $h_m$  [ $Wm^{-2}K^{-1}$ ], heat flux  $q_m$  [ $Wm^{-2}$ ], and local ambient temperature  $T_{\infty m}$ .

The temperature is driven by three causative functions: internal heating g; initial condition  $T_0$ ; and, boundary heating  $(h_m T_{\infty m} + q_m)$ . Here the boundary heating is a generalized condition which provides for three types of boundary heating conditions depending on the values of  $h_m$  and  $q_m$  [42]. For nonhomogeneous type 3 (Robin) boundary take  $q_m = 0$ . For boundary heating of type 2 (Neumann), take  $h_m = 0$  and  $q_m \neq 0$ . For the nonhomogeneous type 1 (Dirichlet) boundary, divide Eq. (2) by  $h_m$  and take the limit as  $h_m \to \infty$ , as follows:

$$\underbrace{\frac{1}{h_m} \frac{\partial T}{\partial n_m}}_{=0} + T = T_{\infty m} + \underbrace{\frac{q_m}{B_m}}_{=0} \quad (m^{th} \text{ boundary of R})$$
 (4)

This is a nonhomogeneous type 1 condition on the  $m^{th}$  boundary.

This problem will be made dimensionless with the following variables:

$$\tilde{T} = \frac{T - T_{\infty}}{T_1 - T_{\infty}}; \quad \tilde{t} = \frac{\alpha t}{L^2}; \quad \tilde{\mathbf{r}} = \frac{\mathbf{r}}{L}; \quad \tilde{n}_m = \frac{n_m}{L}; \quad B_m = \frac{h_m L}{k}$$

$$\tilde{q}_m = \frac{q_m L}{k T_1}; \quad \tilde{g} = \frac{g L^2}{k T_1}$$
(5)

Here L [m] is a length scale and  $T_1$  [K] is a temperature scale. Introduce the above variables for the normalized temperature problem:

$$\frac{\partial \tilde{T}}{\partial \tilde{t}} = \tilde{\nabla}^2 \tilde{T} + \tilde{g}(\tilde{\mathbf{r}}, \tilde{t}) \text{ (domain R)}$$
 (6)

$$\frac{\partial \tilde{T}}{\partial \tilde{n}_m} + B_m \tilde{T} = B_m \tilde{T}_{\infty m} + \tilde{q}_m \ (m^{th} \text{ boundary of R})$$
 (7)

$$\tilde{T}(\tilde{\mathbf{r}}, \tilde{t} = 0) = \tilde{T}_0(\tilde{\mathbf{r}})$$
 (initial condition) (8)

Because the boundary value problem for temperature is linear, the GF solution equation for the temperature is the sum of three terms:

$$\tilde{T}(\mathbf{r},t) = \tilde{T}_{in}(\mathbf{r},t) + \tilde{T}_{g}(\mathbf{r},t) + \tilde{T}_{bc}(\mathbf{r},t)$$
(9)

Quantity  $\tilde{T}_{\rm in}$  is the temperature contribution from the initial condition,  $\tilde{T}_g$  is from internal (volumetric) heating, and  $\tilde{T}_{\rm bc}$  is from the nonhomogeneous boundary conditions. In Table 1 the expression for each of these three terms is given for the analytical GF solution [7, chap. 3] and by analogy, for the discrete GF solution. The entries in Table 1 will be discussed one at a time.

**Table 1** Temperature expressions with the continuous GF and with the discrete GF, with contributions to temperature caused by: initial condition  $\tilde{T}_{\rm in}$ ; internal heating  $\tilde{T}_{\rm g}$ ; and, boundary conditions  $\tilde{T}_{\rm bc}$ .

	Continuous GF	Discrete GF
$ ilde{T}_{ m in}$ $ ilde{T}_{ m g}$ $ ilde{T}_{ m bc}$	$\int_{R} G _{\tau=0} \tilde{T}_{0}(\mathbf{r}') dV'$ $\int_{\tau=0}^{t} \int_{R} G\tilde{g}(\mathbf{r}', \tau) dV' d\tau$ $\int_{\tau=0}^{t} \int_{A_{m}} G _{\mathbf{r}'_{m}} (B_{m}\tilde{T}_{\infty m} + \tilde{q}_{m}) dA'_{m} d\tau$	$\mathbf{G} _{ au=0}\mathbf{ ilde{T}}_0$ $\int_0^t \mathbf{G}\mathbf{ ilde{g}}d au$ $\int_0^t \mathbf{G}\mathbf{ ilde{g}}_md au$ , where
	$J\tau = 0 JA_m$	$\tilde{\mathbf{g}}_{m} = \left(B_{m}\tilde{\mathbf{T}}_{\infty m} + \tilde{\mathbf{q}}_{m}\right)\frac{\tilde{A}_{m}}{\tilde{V}_{m}}$

The first row of Table 1 shows the contribution to temperature from a non-zero initial condition. To discern the discrete temperature expression from the continuous temperature expression, the spatial integral in the continuous temperature expression is replaced by the discrete GF matrix multiplied by the initial temperature vector  $\tilde{\mathbf{T}}_0$ . This matrix multiplication insures that all nodes with non-zero initial condition have an impact on the resulting temperature.

The second row of Table 1 gives the contribution to the temperature caused by internal heat generation, and as for the first row, the spatial integral from the continuous temperature expression is replaced by the GF matrix multiplied by the causative effect, this time the internal heating vector  $\tilde{g}$  to produce the discrete temperature expression. Vector  $\tilde{g}$  may vary in space and in time.

The third row of Table 1 gives the contribution to temperature for heating at the boundary. For the continuous GF method, there is a surface integral involving the GF evaluated at the boundary  $\tilde{\mathbf{r}}' = \tilde{\mathbf{r}}'_m$ , multiplied by the boundary heat flux  $(B_m \tilde{T}_{\infty m} + \tilde{q}_m)$ . This surface integral is developed from a volume integral using Green's theorem. In contrast, the discrete GF can only be evaluated at node locations, which may or not be located at the boundary. To construct the discrete temperature expression for boundary heating, the surface integral from the continuous temperature expression is replaced by the GF matrix multiplied by an n-vector  $\tilde{\mathbf{g}}_m$  whose elements are non-zero only at boundary nodes where heating takes place. The elements of vector  $\tilde{\mathbf{g}}_m$  are given by

$$\tilde{\mathbf{g}}_{m} = \begin{cases} \left(B_{m}\tilde{\mathbf{T}}_{\infty m} + \tilde{\mathbf{q}}_{m}\right)\tilde{A}_{m}/\tilde{V}_{m}; & \text{node } m \text{ on boundary} \\ 0; & \text{otherwise} \end{cases}$$
(10)

which represent the equivalent volumetric heating caused by heating at boundary nodes. That quantity  $\tilde{\mathbf{g}}_m$  should contain the ratio  $A_m/V_m$  can be demonstrated by equating the energy added to a node by volume generation g to that added by boundary heat flux g:

$$g \cdot V = q \cdot A$$
, or,  $g = q \cdot \frac{A}{V}$  (11)

This energy balance states that the equivalent volumetric generation [W  $m^{-3}$ ] is equal to the applied heat flux [W  $m^{-2}$ ] times area [ $m^2$ ] divided by nodal volume [ $m^3$ ].

The discrete GF solution equation provides a comprehensive and systematic approach for a family of solutions with a variety of heating conditions, once the discrete GF is known. In the following section, the discrete GF is developed from the spectral graph method

#### 2.2. Spectral graph method for the discrete Green's function

The Green's function will be found as the solution to an initial-condition problem with homogeneous boundary conditions, which is a standard approach [7, p. 28]. However here the spectral graph method will be applied to the heat equation, by replacing the

Laplacian operator  $(\tilde{\nabla}^2)$  with a discrete operator called the Laplacian matrix (L). Also the continuous temperature is replaced by a vector of discrete temperatures  $(\tilde{\mathbf{T}})$  at node points in the domain. The discrete form of the heat diffusion equation, with homogeneous boundary conditions and specified initial condition, may be written as

$$\frac{\partial \tilde{\mathbf{T}}_{in}}{\partial \tilde{t}} = -\mathbf{L}\tilde{\mathbf{T}}_{in} \qquad \text{(domain R)}$$

$$\frac{\partial \tilde{\mathbf{T}}_{in}}{\partial \tilde{n}_m} + B_m \tilde{\mathbf{T}}_{in} = 0 \qquad (m^{th} \text{ boundary of R})$$
 (13)

$$\tilde{\mathbf{T}}_{in}\big|_{\tilde{t}=0} = \tilde{\mathbf{T}}_0$$
 (initial condition) (14)

Note the sign change in Eq. (12), as the Laplacian matrix  ${\bf L}$  from graph theory is defined with sign opposite to that of the continuous Laplacian operator ( $\tilde{\bf V}^2$ ). A contribution of the present work is the type 3 boundary condition in Eq. (13); although elements of the following development are similar to our previous work with the type 2 (insulated) boundary [2], the present analysis goes further to define the discrete Green's function. For the moment we assume that the Laplacian matrix satisfies the type 3 boundary condition; internal details of this Laplacian matrix are developed later in Section 2.3.

The next step is to solve an eigenvalue problem using standard matrix methods. Laplacian matrix  ${\bf L}$  satisfies the following eigenvalue equation:

$$\mathbf{L}\phi = \phi\Lambda \tag{15}$$

where  $\phi$  is the orthogonal eigenvector matrix

 $\Lambda$  is the diagonal eigenvalue matrix

The eigenvector matrix  $\phi$  is orthogonal because **L** is symmetric and diagonally dominant [11]. Since for an orthogonal matrix the transpose is equal to its inverse, the product of the eigenvector matrix and its transpose is the identity matrix. That is:

$$\phi \phi' = \phi \phi^{-1} = \mathbf{I} \tag{16}$$

Using this property, post-multiply the eigenvalue equation, Eq. (15), by the matrix  $\phi'$ :

 $\mathbf{L}\phi\phi'=\phi\Lambda\phi'$ 

$$\mathbf{LI} = \phi \Lambda \phi'$$

$$\mathbf{L} = \phi \Lambda \phi'$$
(17)

Replace this result into the discrete diffusion equation, Eq. (12):

$$\frac{\partial \tilde{\mathbf{T}}_{in}}{\partial \tilde{t}} = -(\phi \Lambda \phi') \tilde{\mathbf{T}}_{in} \tag{18}$$

This above equation is a first order matrix differential equation whose solution has the form of a matrix exponential [10,11]:

$$\tilde{\mathbf{T}}_{in} = e^{-\phi \Lambda \phi' \tilde{t}} \tilde{\mathbf{T}}_{0} \tag{19}$$

Recall that  $\tilde{\mathbf{T}}_0$  is the initial temperature vector. Next the exponential in the above solution will be expanded using a Taylor series. The exponential of matrix u is given by

$$e^{-u} = \mathbf{I} - \frac{u}{1!} + \frac{u^2}{2!} - \frac{u^3}{3!} + \dots$$

Apply the above Taylor series expansion to the exponential term from Eq. (19), and simplify:

$$\begin{split} e^{-\phi \Lambda \phi' \tilde{t}} &= \boldsymbol{I} - \tilde{t} \frac{\phi \Lambda \phi'}{1!} + \tilde{t}^2 \frac{(\phi \Lambda \phi')^2}{2!} - \tilde{t}^3 \frac{(\phi \Lambda \phi')^3}{3!} + \dots \\ &= \boldsymbol{I} - \tilde{t} \frac{\phi \Lambda \phi'}{1!} + \tilde{t}^2 \frac{(\phi \Lambda \phi')(\phi \Lambda \phi')}{2!} \end{split}$$

$$-\tilde{t}^{3} \frac{(\phi \Lambda \phi')(\phi \Lambda \phi')(\phi \Lambda \phi')}{3!} + \dots$$

$$= \mathbf{I} - \frac{\phi(\Lambda \tilde{t}) \phi'}{1!} + \frac{(\phi(\Lambda \tilde{t})^{2} \phi')}{2!} - \frac{(\phi(\Lambda \tilde{t})^{3} \phi')}{3!} + \dots$$

$$= \phi \left[ \mathbf{I} - \frac{\Lambda \tilde{t}}{1!} + \frac{(\Lambda \tilde{t})^{2}}{2!} - \frac{(\Lambda \tilde{t})^{3}}{3!} + \dots \right] \phi'$$

$$= \phi \left[ e^{-\Lambda \tilde{t}} \right] \phi'$$
(20)

The final exponential argument contains only the eigenvalue matrix multiplied by time. With this simplification the temperature solution (Eq. 19) is given by

$$\tilde{\mathbf{T}}_{in} = \phi e^{-\Lambda \tilde{t}} \phi' \, \tilde{\mathbf{T}}_0 \tag{21}$$

In this solution, the spatial behavior is embodied in the eigenfunction matrix  $\phi$  and the time-evolution behavior is embodied in the eigenvalue matrix  $\Lambda$ .

Next the above solution is compared to that from the GF approach. Assuming for the moment that the GF is known, the solution to the discrete initial-temperature problem (Eq. 12 - 14) is constructed by multiplying the GF by the initial temperature  $\tilde{\mathbf{T}}_0$  as given in the first row of Table 1:

$$\tilde{\mathbf{T}}_{in} = \mathbf{G}|_{\tau=0} \ \tilde{\mathbf{T}}_0 \tag{22}$$

Here  $\mathbf{G}|_{\tau=0}$  is the discrete GF evaluated at heating time  $\tau=0$ . Now compare the formal statement of the discrete GF solution in Eq. (22) to the spectral graph solution given in Eq. (21). As the solution to a boundary value problem is unique, the discrete GF evaluated at  $\tau=0$  must be

$$\mathbf{G}|_{\tau=0} = \phi e^{-\Lambda \tilde{t}} \phi' \tag{23}$$

The final step is to recognize that the time behavior of every GF for the heat equation has functional form  $(t-\tau)$  where t is the observation time and  $\tau$  is the heating time [7, p. 37]. Then the discrete GF for  $\tau \neq 0$  is given by:

$$\mathbf{G} = \phi e^{-\Lambda(\tilde{t} - \tilde{\tau})} \phi' \tag{24}$$

This is the discrete GF, in the form of a matrix, as provided by the spectral graph (SG) method. The discrete GF satisfies a (discrete) boundary value problem with homogeneous boundary conditions and impulsive initial condition. One column of the GF matrix contains the temperature response to a unit-impulse initial condition at one node; all the columns together provide the comprehensive response.

The above GF matrix was developed assuming that the Laplacian matrix is known, has well-behaved eigenvectors and eigenvalues, and satisfies type 3 boundary conditions that are homogeneous. In the next section the details of the Laplacian matrix are developed.

# 2.3. Energy balance for a node at a convection boundary

In this section the required Laplacian matrix is constructed from the node equations for the discrete form of the heat conduction equation. The node equations are found from an energy balance using the finite-volume theory of Patankar [43]. A node at the boundary is examined with convection heat loss, and then the result for a non-boundary (interior) node is a straightforward special case.

The discussion begins with the energy balance on the element containing node i at temperature  $T_i$  shown in Fig. 1. The sum of the heat flow into element i is equal to the energy storage in the element:

$$\sum Q = CV_i \frac{\partial T_i}{\partial t} \tag{25}$$

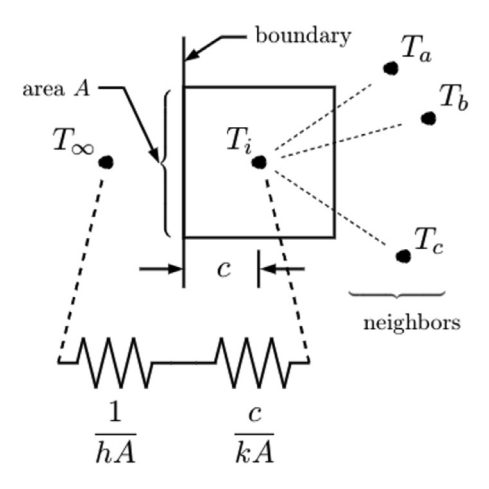


Fig. 1. Boundary node with thermal resistance for heat loss to surroundings at  $T_{\infty}$ .

Here Q [W] is heat flow into the element, C is volumetric specific heat [J m<sup>-3</sup> K],  $V_i$  is element volume [m<sup>3</sup>], and t is time [s]. The energy storage is proportional to the time-rate-of-change of temperature in the element,  $T_i$ . The heat flow may come from neighbor nodes or it may come through the boundary. The heat flow coming from the jth neighbor node is given by

$$Q_j = w_{ij}(T_j - T_i) (26)$$

where

 $T_i$  ... temperature of node i of interest [K]

 $T_i$  ... temperature of neighbor node j [K]

 $w_{ij}$  ... edge weight between nodes i and j [W K<sup>-1</sup>]

It is important to note that edge weights are non-zero only for near-neighbor nodes, and they depend only on the distance between nodes. More information on edge weights is given later in Section 2.4.

The heat flow from the boundary into node i is found from the thermal resistance:

$$Q = \frac{T_{\infty} - T_i}{R_i} \tag{27}$$

where

 $T_{\infty}$  ... ambient temperature [K]

 $R_i$  ... total thermal resistance at boundary [K W<sup>-1</sup>]

The thermal resistance is the sum of two thermal resistors, shown in Fig. 1:

$$R_i = \frac{1}{h_i A_i} + \frac{c_i}{k A_i} \tag{28}$$

where  $h_i$  is the heat transfer coefficient [W m<sup>-2</sup> K<sup>-1</sup>],  $A_i$  is the area for boundary heat transfer [m<sup>2</sup>],  $c_i$  [m] is distance from node i to the boundary as shown in Fig. 1, and k is thermal conductivity [W m<sup>-1</sup> K<sup>-1</sup>]. Heat transfer coefficient  $h_i$  is an effective value that includes both convective and linearized radiative contributions; nonlinear boundary conditions are not included here. Replace the two types of heat flow into Eq. (25) to find the boundary node heat balance:

$$\sum_{i=1}^{n} w_{ij} (T_j - T_i) + \frac{T_\infty - T_i}{R_i} = CV_i \frac{\partial T_i}{\partial t}$$
(29)

where n is the number of nodes in the body. Although the sum in the above expression is shown over all the nodes in the body, weights  $w_{ij}$  are non-zero only for near-neighbor nodes.

#### 2.3.1. Normalized energy balance

The node equation will be normalized with the following dimensionless variables:

$$\tilde{T} = \frac{T - T_{\infty}}{T_1 - T_{\infty}}; \quad \tilde{t} = \frac{kt}{CL^2}; \quad \tilde{w}_{ij} = \frac{w_{ij}L^2}{kV_i} 
\tilde{A}_i = \frac{A_i}{L^2}; \quad \tilde{V}_i = \frac{V_i}{L^3}; \quad \tilde{c}_i = \frac{c_i}{L}; \quad B_i = \frac{h_i L}{k}$$
(30)

where  $T_1$  is a characteristic temperature [K] and L is a characteristic global length [m], and  $B_i$  is the Biot number describing heat loss at the boundary. Replace these dimensionless variables into Eq. (25), use the definition of resistance  $R_i$  from Eq. (28), and after some algebra, the boundary node heat balance takes the form

$$\sum_{j=1}^{n} \tilde{w}_{ij} (\tilde{T}_{j} - \tilde{T}_{i}) - \tilde{E}_{i} \tilde{T}_{i} = \frac{\partial \tilde{T}_{i}}{\partial \tilde{t}}$$
(31)

where 
$$\tilde{E}_i = \frac{\tilde{A}_i}{\tilde{V}_i} \left( \frac{B_i}{1 + B_i \tilde{c}_i} \right)$$
 (32)

Here  $\tilde{E}_i$  is a dimensionless conductance for heat loss when node i is located at a type 3 boundary. Note the sign change on this boundary term, which comes from the definition of the normalized temperature. Finally, separate those terms involving neighbor temperatures from the temperature at the ith node:

$$\sum_{j=1}^{n} \tilde{W}_{ij} \tilde{T}_{j} - \sum_{j=1}^{n} \tilde{W}_{ij} \tilde{T}_{i} - \tilde{E}_{i} \tilde{T}_{i} = \frac{\partial \tilde{T}_{i}}{\partial \tilde{t}}$$
(33)

In the above expression the labels 'diagonal' and 'off diagonal' identify the locations of these terms in the ith row of the Laplacian matrix when the ith node is at a type 3 boundary. For non-boundary nodes, or for nodes on insulated boundaries, the development is identical, except that there is no external heat flow. That is, set  $\tilde{E}_i = 0$  at interior nodes, then the heat balance is given by

$$\sum_{j=1}^{n} \tilde{w}_{ij} \tilde{T}_{j} - \sum_{j=1}^{n} \tilde{w}_{ij} \tilde{T}_{i} = \frac{\partial \tilde{T}_{i}}{\partial \tilde{t}} \quad \text{(interior node)}$$
(34)

off diagonal diagonal

#### 2.3.2. Details of the Laplacian matrix

In this section the Laplacian matrix is assembled from the energy balance relations at each node. The Laplacian matrix is the discrete matrix that replaces the spatial derivatives when the continuous heat equation is replaced by the discrete heat equation. The discrete heat equation is given by Eq. (12):

$$-\mathbf{L}\tilde{\mathbf{T}} = \frac{\partial \tilde{\mathbf{T}}}{\partial \tilde{t}} \tag{35}$$

Recall that L is the Laplacian matrix and  $\tilde{T}$  is the (dimensionless) temperature vector. Next write out the full matrix form of the above energy equation, as follows:

$$-\begin{bmatrix} L_{11} & L_{12} & \cdots & L_{1n} \\ L_{21} & L_{22} & \cdots & L_{2n} \\ \vdots & & \ddots & L_{n-1,n} \\ L_{n1} & \cdots & L_{n,n-1} & L_{nn} \end{bmatrix} \begin{bmatrix} \tilde{T}_1 \\ \tilde{T}_2 \\ \vdots \\ \tilde{T}_n \end{bmatrix} = \frac{\partial}{\partial \tilde{t}} \begin{bmatrix} \tilde{T}_1 \\ \tilde{T}_2 \\ \vdots \\ \tilde{T}_n \end{bmatrix}$$
(36)

Next, consider the *i*th row of the above expression, and compare it to the node equations given earlier for boundary nodes (Eq. 33) and for interior nodes (Eq. 34). A careful examination shows that the elements of the Laplacian matrix have the following form:

$$L_{ij} = \begin{cases} -\tilde{W}_{ij}; & i \neq j \\ \sum_{j=1}^{n} \tilde{W}_{ij} + \tilde{E}_{i}; & i = j \end{cases}$$

$$(37)$$

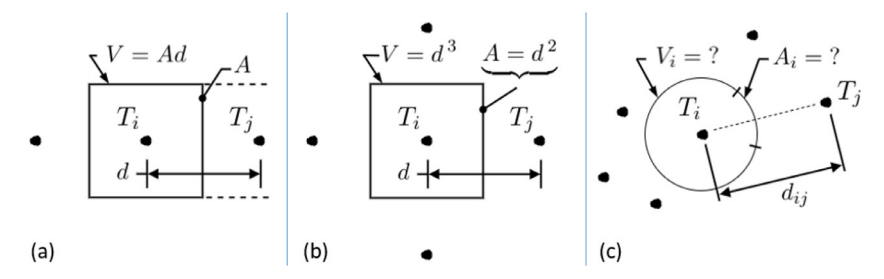


Fig. 2. Geometry for heat flow between nodes for (a) 1-D uniform grid (b) 3-D uniform rectangular grid (c) 3-D random grid.

Recall that  $\tilde{E}_i \neq 0$  only for nodes located on a boundary exchanging heat with the surroundings.

The above Laplacian matrix was developed from an energy balance. The addition of the heat-loss term  $\tilde{E}_i$  at boundary nodes is a unique contribution of the present work; without this term the above development is equivalent to the usual graph theory approach involving an adjacency matrix and a diagonal matrix [10,11].

#### 2.4. Physics-based edge weights

Edge weights  $\tilde{w}_{ij}$  were defined earlier in Eq. (26) as  $Q=w_{ij}(T_j-T_i)$ . The edge weight multiplies a temperature difference to give the heat flow. The edge weights developed here are consistent with the finite volume method of Patankar [43]. For heat transfer in a solid body, the heat flow rate from node j to node i is given by

$$Q = \frac{kA_{ij}}{d_{ij}}(T_j - T_i) \tag{38}$$

The heat flow rate depends on the conductivity k [W m<sup>-1</sup>K<sup>-1</sup>], the area for heat flow  $A_{ij}$  [m<sup>2</sup>], and the distance between the nodes  $d_{ij}$  [m]. Then the edge weights are given by

$$w_{ij} = \frac{kA_{ij}}{d_{ij}}$$
 or,  $\tilde{w}_{ij} = \frac{\tilde{A}_{ij}}{\tilde{d}\tilde{V}_i}$  (39)

The normalized edge weight is constructed using the normalized variables in Eqn 30, where  $\tilde{V}_i$  is the (normalized) small volume associated with node i. To fully specify the edge weight, geometric information on the nodal grid is required to determine ratio  $\tilde{A}_{ij}/\tilde{V}_i$ . Three grid geometries are discussed below.

#### 2.4.1. 1-D uniform grid.

In the one-dimensional uniform grid, the node spacing and the heat transfer area is the same for every pair of adjacent nodes. Refer to Fig. 2a for a schematic of the 1-D uniform grid. Let  $\tilde{d}$  be the (normalized) node spacing and let  $\tilde{A}$  be the (normalized) heat transfer area, so that the nodal volume is given by  $\tilde{V} = \tilde{A}\tilde{d}$ . Then the edge weights are given by

$$\tilde{w}_{ij} = \frac{\tilde{A}_i}{\tilde{d}\tilde{A}_i\tilde{d}} = \frac{1}{\tilde{d}^2} \tag{40}$$

These edge weights are identical to the temperature coefficients used in the finite difference method, which means that the one-dimensional SG method and the one-dimensional finite difference method have the same spatial behavior [2].

# 2.4.2. 3D Uniform rectangular grid.

In the 3-D uniform rectangular grid shown in Fig. 2b, the node spacing and the heat transfer area is the same for every pair of adjacent nodes, and the volume associated with node i is a small cube. Let  $\tilde{d}$  be the (normalized) node spacing, let  $\tilde{A} = \tilde{d}^2$  be the

area for heat transfer, and let  $\tilde{V}=\tilde{d}^3$  be the nodal volume. Then the edge weights are given by

$$\tilde{w}_{ij} = \frac{\tilde{d}^2}{\tilde{d}\tilde{d}^3} = \frac{1}{\tilde{d}^2} \tag{41}$$

which are identical to the 1-D case.

#### 2.4.3. 3-D random grid.

In the 3-D random grid shown in Fig. 2c, the edge weight depends upon the details of the geometric relationships among all of the nodes surrounding node *i*. In the spectral graph method, however, it is important that the edge weights depend primarily on the internodal distance, rather than on geometric details. In the authors' previous work, the edge weights for the 3-D random grid had an exponential form, drawn from image processing applications, as follows

$$\tilde{w}_{ij} = \begin{cases} f \exp\left(-\frac{\tilde{d}_{ij}^2}{\sigma^2}\right); & \tilde{d}_{ij} < r_n \\ 0; & \tilde{d}_{ij} \ge r_n, \text{ and } i = j \end{cases}$$

$$(42)$$

Quantity  $\sigma$  is the standard deviation of all lengths  $d_{ij}$ . Quantity f is the gain factor and  $r_n$  is the neighbor radius, and these two quantities need to be chosen through a calibration process for the method to provide good results. This approach provided reasonable precision with very low computation cost for mesh generation.

In the present work, edge weights for the 3-D random grid were sought that are based on the physics of the problem yet were compatible with the spectral graph method. Edge weights were sought that would: depend on internodal distance  $\tilde{d}_{ij}$ ; build upon our experience with exponential weights used previously; avoid dependence on local ratio  $\tilde{A}_{ij}/\tilde{V}_i$ ; and; reduce to  $1/\tilde{d}_{ij}^2$  in the limit as the random grid moves toward a uniform rectangular grid.

This last requirement suggested that a simple yardstick was needed to determine when a given grid deviates from the uniform rectangular grid. The average distance between adjacent nodes is defined

$$\ell = \left(\frac{V_{tot}}{n}\right)^{1/3}.\tag{43}$$

Quantity  $\ell$  may be viewed as the width of a cube containing the average nodal volume; for a uniform rectangular grid  $\ell$  is the exactly the distance between nearest nodes. With quantity  $\ell$ , the following edge weights satisfy the above constraints:

$$\tilde{w}_{ij} = \begin{cases} \frac{f}{\ell^2} \exp\left(\frac{\ell^2 - \tilde{d}_{ij}^2}{\sigma^2}\right); & \tilde{d}_{ij} < \sqrt{2}\,\ell\\ 0; & \tilde{d}_{ij} \ge \sqrt{2}\,\ell, \text{ and } i = j \end{cases}$$

$$(44)$$

These physics-based edge weights have several important features. First, in the limit as distance  $d_{ij}$  approaches the average nodal distance  $\ell$ , the exponential becomes unity and the edge weight has functional form  $1/\ell^2$  which is in agreement with the energy-conserving finite volume formulation. Therefore this expression for

the edge weights applies to every geometry. Second, radius  $\sqrt{2}\,\ell$  defines a sphere which provides a small number of nearest neighbors; this would be six neighbors for a uniform rectangular grid (for an interior node). In contrast, in previous work the nearest neighbors were defined by an independently-chosen neighbor radius. The present work has linked the neighbor radius to the number of nodes, thus reducing the number of calibration parameters from two to one which simplifies the calibration process. Third, because the edge weights are scaled by length  $\ell$  which depends on the number of nodes, the calibration may be carried out on one grid and the calibration does not have to be repeated if the node count is changed, for example, as part of a grid refinement study.

Quantity  $\tilde{E}_i$  for boundary heat loss, defined in Eq. (32), must also be determined, which depends upon the nodal surface area for external heat loss  $A_m$ . Although the details of the body shape could be used to provide a precise surface area  $A_m$  for each surface node, this is not consistent with the geometry-blind edge weights discussed above. Instead an average external surface area is used, the same for each boundary node, defined by the overall surface area of the body, divided by the number of surface nodes. This is congruent with the goal of the present work for rough and rapid thermal simulations, as distinct from FE solutions, which require burdensome meshing calculations. This approach is most accurate for bodies with high node counts and generous fillets, and the level of approximation increases as the node count decreases and the fillet radius decreases.

#### 2.5. Discrete in space, analytic in time

Through the discrete GF, the spectral graph method has been extended to provide for internal heating, with heating at the boundary treated as a special case of internal heating. The temperature expression for internal heating contains a time integral, which is discussed here to demonstrate that the spectral graph method is discrete in space and analytic in time.

Consider an internal heating function  $\tilde{\mathbf{g}}$  which produces a temperature response described by the time integral given in Table 1. Into this time integral substitute the spectral graph form of the GF matrix given by Eq. (24), to find

$$\tilde{\mathbf{T}}_{g}(\tilde{\mathbf{r}}, \tilde{t}) = \int_{\tau=0}^{t} \phi e^{-\Lambda(\tilde{t}-\tilde{\tau})} \phi' \, \tilde{\mathbf{g}} \, d\tilde{\tau} \tag{45}$$

The ease or difficulty in evaluating this time integral depends on the time behavior of internal heating function  $\tilde{\mathbf{g}}$ . In the special case of **time invariant internal heating**, then the time integral may be evaluated in closed form. Recall that the eigenvector matrix  $\phi$  is a function of space, not of time. Then eigenvector matrix  $\phi$  and its transpose may be removed from the time integral, and the time integral may be evaluated as follows:

$$\tilde{\mathbf{T}}_{g}(\tilde{\mathbf{r}}, \tilde{t}) = \phi \left[ \int_{\tau=0}^{t} e^{-\Lambda(\tilde{t}-\tilde{\tau})} d\tilde{\tau} \right] \phi' \, \tilde{\mathbf{g}} 
= \phi \left[ \Lambda^{-1} (\mathbf{I} - e^{-\Lambda \tilde{t}}) \right] \phi' \, \tilde{\mathbf{g}} 
= \phi \, \Lambda^{-1} \phi' \, \tilde{\mathbf{g}} - \phi \, \Lambda^{-1} e^{-\Lambda \tilde{t}} \phi' \, \tilde{\mathbf{g}}; \quad \tilde{\mathbf{g}} \neq \tilde{\mathbf{g}}(\tilde{t}) \quad (46)$$

Here the temperature expression is the sum of a steady part and a complementary transient part. Consequently, the above solution does not apply if the steady solution does not exist, for example, if all the boundaries are insulated (Neumann type). In this circumstance the smallest eigenvalue is zero so that the inverse of the eigenvalue matrix  $(\Lambda^{-1})$  does not exist. There are techniques for dealing with this zero-eigenvalue problem which will not be discussed here in the interest of brevity; see for example [44, p. 164].

A closed-form solution may also be found for heating that is piecewise constant in time. Suppose the internal heating function

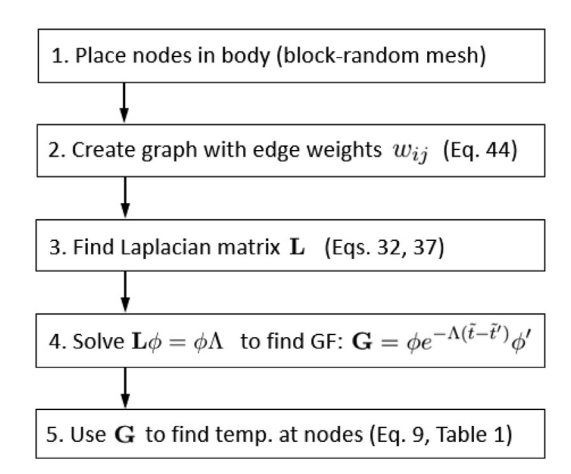


Fig. 3. Steps to carry out the discrete GF method for temperature simulation.

varies in space and is on-off in time, given by

$$\tilde{\mathbf{g}} = \begin{cases} \tilde{\mathbf{g}}_0(\tilde{\mathbf{r}}), & 0 < \tilde{t} \le \tilde{t}_1 \\ 0, & \tilde{t} > \tilde{t}_1 \end{cases}$$

$$\tag{47}$$

Replace this function into Eq. (45) and the integral may be evaluated to give a piecewise-constant-in-time temperature response:

for  $\tilde{t} \leq \tilde{t}_1$ :

$$\tilde{\mathbf{T}}_{g}(\tilde{\mathbf{r}}, \tilde{t}) = \phi \ \Lambda^{-1} (\mathbf{I} - e^{-\Lambda \tilde{t}}) \phi' \ \tilde{\mathbf{g}}_{0}(\tilde{\mathbf{r}})$$

for  $\tilde{t} > \tilde{t}_1$ :

$$\tilde{\mathbf{T}}_{g}(\tilde{\mathbf{r}}, \tilde{t}) = \phi \ \Lambda^{-1} \left( e^{-\Lambda(\tilde{t} - \tilde{t}_{1})} - e^{-\Lambda \tilde{t}} \right) \phi' \ \tilde{\mathbf{g}}_{0}(\tilde{\mathbf{r}})$$
(48)

This solution may be used as a building block to construct the response to any piecewise-constant-in-time heating function, which has application for simulation of a variety of manufacturing processes such as laser welding [45].

#### 2.6. Overview of the discrete GF method

The development of the discrete GF method given above was organized according to mathematical and physical principles. However, the steps needed to carry out a temperature simulation have a somewhat different order, as shown in Fig. 3.

The first step is to distribute nodes throughout the body of interest, and a block-random distribution is recommended for the additive manufacturing application. Next the nodes are connected with edge weights (Eq. 44) to construct a graph. The Laplacian matrix is constructed next, using the energy balance at each node (Eq. 37), taking care to include any heat loss at boundary nodes (Eq. 32). The eigenvalue problem for the Laplacian matrix (Eq. 15) is then solved using standard methods, and the eigenvectors and eigenvalues are used to construct the discrete GF (Eq. 24). Finally, the discrete GF equation (Eq. 9 and Table 1) is used to assemble the temperature response caused by the heating effects which are present in the problem. As long as the spatial geometry does not change, the same discrete GF may be used to find the temperature response to a variety of heating conditions.

#### 2.6.1. Limitations of the method

There are some limitations specific to the discrete GF method. The temperature problem must be linear, so that the material properties must not be functions of the temperature. In practice this means that the properties are evaluated at an effective value during each heating cycle. Actual thermal properties vary with temperature, and to approximately address this non-linear effect, the thermal properties could be iteratively adjusted in response to the calculated temperature. Such iteration has not been attempted.

In the present embodiment of the spectral graph method, the Laplacian matrix is symmetric so that the eigenvalues are real (not complex) and non-negative. This requires that the edge weights are symmetric  $w_{ij}=w_{ji}$ , consequently spatial variation in the material properties is not accommodated. Further, spatial variation in the node density is ruled out because the present approach assumes that each node, on average, represents the same volume subset  $V_i$ . A point of future work is to relax this limitation on spatial variation of nodal properties which, combined with iteration, could be used to address temperature dependent thermal properties. A related point for future work is to lower the node count in regions where thermal gradients are low, to increase computational speed with minimal impact on precision.

There are other sources of uncertainty that are present in all thermal simulation methods. The precision depends strongly on the node density in the body, and this effect is quantified in examples given later in Section 3. There is uncertainty in the amount of heat loss at the boundaries, that is, uncertainty in the boundary heat transfer coefficient. Additionally for laser heating which is one motivation for the present work, there is uncertainty in the amount of energy actually absorbed during the process. To address such uncertainties, comparison with experiments is needed to determine the heat budget, heat in and heat out. A consequence of experimental calibration is that although the shape of the temperature history will be imperfect (from imperfect thermal properties or low node density, for example), the end point of the temperature history may closely match the experiment.

#### 2.6.2. Relation to separation of variables method

The discrete GF method has some elements in common with the separation of variables (SOV) method. In both methods the coefficients of the heat equation and the boundary conditions must be constant, that is, the problem must be linear in temperature. In both methods the solution contains a product of a spatially-dependent function and a time-dependent one. In both methods a standard procedure for finding a basic solution is through an initial-value problem. The discrete GF contains an exponential on time  $e^{-\Lambda(\tilde{l}-\tilde{r})}$ , so that at small time, many eigenvalues are active in determining the temperature. This is analogous to the many series terms needed in an SOV solution at small values of time. The number of eigenvalues available in the discrete GF method is equal to the number of nodes in the body, consequently the grid spacing determines the smallest time for which the temperature can be obtained without degradation of precision.

A point of difference is that the SOV method applies only to simple body shapes for which the boundaries are defined by a constant value of one coordinate (orthogonal body), but the discrete GF method applies to any body shape. Finally, the SOV method is fully analytical so the temperature may be found at any time and at any spatial location. For the discrete GF method the temperature may also be found at any value of the time (analytic in time), however temperature is provided only at node locations (discrete in space).

# 3. Verification by comparison with exact solutions

In this section examples are given for heat diffusion in bodies with plane surfaces for which exact analytical solutions are available, and the exact solutions are compared with numerical results from the improved spectral graph method. The first example is a slab body heated internally in an on-off fashion, and the second example is a three dimensional body (parallelepiped) with a piecewise initial condition.

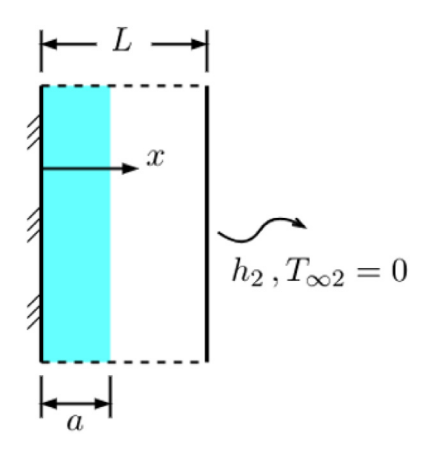


**Fig. 4.** Schematic of problem X23B00G(x5t5)T0, the slab with on-off internal heating over region (0 < x < a) with one insulated boundary and one convection boundary.

#### 3.1. Example 1. Slab body with on-off internal heating

Consider the following 1D problem with on-off internal heating that is piecewise in space, with one boundary insulated, and with convection heat loss from the other boundary:

$$\frac{\partial \tilde{T}}{\partial \tilde{t}} = \frac{\partial^2 \tilde{T}}{\partial \tilde{x}^2} + \tilde{g}(\tilde{x}, \tilde{t}) \tag{49}$$

at 
$$\tilde{x} = 0$$
,  $\frac{\partial \tilde{T}}{\partial \tilde{x}} = 0$   
at  $\tilde{x} = 1$ ,  $k \frac{\partial \tilde{T}}{\partial \tilde{x}} + B_2 \tilde{T} = 0$   
at  $\tilde{t} = 0$ ,  $\tilde{T}(\tilde{x}, 0) = 0$   
and where  $\tilde{g}(\tilde{x}, \tilde{t}) = \begin{cases} 1; & 0 < \tilde{x} \leq \tilde{a} \text{ and } \tilde{t} \leq \tilde{t}_1 \\ 0; & \text{otherwise} \end{cases}$  (50)

This problem has been normalized with the variables given in Eq. (4). The geometry for this problem is shown in Fig. 4. This problem is denoted case X23B00G(x5t5)T0 in the numbering system for heat conduction [7, chap. 2].

The exact analytic solution to this problem, denoted  $\tilde{T}_{\text{ON-Off}}$  will be assembled from a building-block solution for which the heating is always on, denoted  $\tilde{T}_{\text{ON}}$ . Consider the same problem as above but for always-on internal heating described by

$$\tilde{g}(\tilde{x}) = \begin{cases}
1; & 0 < \tilde{x} \le \tilde{a} \\
0; & \tilde{x} > \tilde{a}
\end{cases}$$
(51)

Then the temperature for the on-off heating problem is given by

$$\tilde{T}_{\text{on-off}}(\tilde{x}, \tilde{t}) = \begin{cases} \tilde{T}_{\text{on}}(\tilde{x}, \tilde{t}); & 0 < \tilde{t} \le \tilde{t}_1 \\ \tilde{T}_{\text{on}}(\tilde{x}, \tilde{t}) - \tilde{T}_{\text{on}}(\tilde{x}, \tilde{t} - \tilde{t}_1); & \tilde{t} > \tilde{t}_1 \end{cases}$$
(52)

The exact analytic solution for building block  $\tilde{T}_{OR}$  is given by [46]

$$\tilde{T}_{on} = \tilde{T}_{ss}(\tilde{x}) + \tilde{T}_{ct}(\tilde{x}, \tilde{t})$$
(53)

where  $\tilde{T}_{SS}$  is the steady state portion of the solution and  $\tilde{T}_{ct}$  is the complementary transient portion of the solution. The steady-state solution is piecewise in space.

For  $x \leq a$ :

$$\tilde{T}_{ss}(x) = \frac{1}{B_1 B_2 + B_1 + B_2} \left[ \left( -\frac{B_1 B_2}{2} - \frac{B_1}{2} - \frac{B_2}{2} \right) \tilde{x}^2 + \left( -\frac{B_1 B_2}{2} \tilde{a}^2 + B_1 B_2 \tilde{a} + B_1 \tilde{a} \right) \tilde{x} + \left( -\frac{B_2 \tilde{a}^2}{2} + B_2 \tilde{a} + \tilde{a} \right) \right]$$
(54)

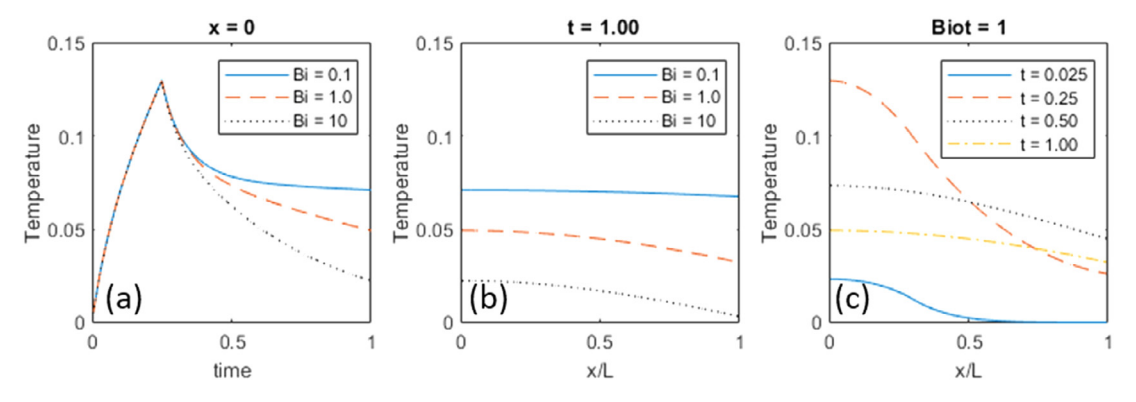


**Fig. 5.** Temperature results for case X23B00G(x5t5)T0 for on-off heating over (0 < x/a < 0.25): (a) temperature at insulated surface x=0; (b) temperature at  $\tilde{t} = 1.0$ ; and, (c) temperature at Biot = 1 at four times.

For x > a:

$$\tilde{T}_{ss}(\tilde{x}) = \frac{1}{B_1 B_2 + B_1 + B_2} \left[ \left( -\frac{B_1 B_2 \tilde{a}}{2} - B_2 \tilde{a} \right) \tilde{x} + \left( \frac{B_1 B_2}{2} \tilde{a}^2 + \frac{B_1}{2} \tilde{a}^2 + B_2 \tilde{a} + B_1 \tilde{a} \right) \right]$$
(55)

The complementary transient portion is given by

$$\tilde{T}_{ct}(\tilde{x}, \tilde{t}) = -\sum_{m=1}^{\infty} \exp(-\beta_m^2 \tilde{t}) [\beta_m \cos(\beta_m \tilde{x}) + B_1 \sin(\beta_m \tilde{x})] \\
\times \frac{\left[\sin(\beta_m \tilde{a}) - \frac{B_1}{\beta_m} \cos(\beta_m \tilde{a}) + \frac{B_1}{\beta_m}\right]}{\beta_m^2 N_m}$$
(56)

where 
$$N_m = \frac{1}{2} \left[ (\beta_m^2 + B_1^2) \left( 1 + \frac{B_2}{\beta_m^2 + B_2^2} \right) + B_1 \right]$$
  
where  $\beta_m$  satisfies  $\tan \beta_m = \frac{\beta_m (B_1 + B_2)}{\beta_m^2 - B_1 B_2}$  (57)

The above solution for  $\tilde{T}_{0\Pi}$  is actually for case X33B00Gx5T0, but the insulated boundary at x = 0 may be obtained from this solution, to high precision, by taking  $B_1$  small, say  $10^{-10}$ .

Some temperature values for Example 1 are shown in Fig. 5 which were computed from the exact solution, Eqs. (52–57) for heating region of size  $\tilde{a}=0.25$  and for heating-off time  $\tilde{t}_1=0.25$ . Figure 5a shows temperature versus time at the x=0 insulated boundary for three values of the Biot number  $B_2$ . Note the temperature for different Biot numbers have the same shape initially, and then the effect of the boundary at x=L causes the curves for different Biot to diverge for  $\tilde{t}>0.4$ . Figure 5b shows the temperature versus position at  $\tilde{t}=1.0$  for three values of the Biot number. Figure 5c shows temperature versus position at four dimensionless times for Biot =1.0. For the first two times the heating is on so temperature is rising; for the last two times the heating is off and the temperature is falling.

Next a comparison is made between temperature values computed from the exact solution, from the SG method, and from a fully implicit finite difference solution [43]. Temperatures from the SG method for this problem were computed from Eq. (48) with Laplacian given in Eq. (37) and edge weights from Eqn 44. In Fig 6 the comparison is made for the specific conditions  $B_2 = 1.0$ , nt = 20, and nx = 20. As before the heated region is of size  $\tilde{a} = 0.25$  and the heating-off time is  $\tilde{t}_1 = 0.25$ . Figs. 6a and 6 b show the temperature, and Figs 6c and 6 d show the relative error  $|T - T_{exact}|/T_{exact}$ . The relative error is used to identify the distance from the exact temperature at a single location in space and time, as a fraction of the exact temperature value. The numerical results are close to the exact values, even though the grid is coarse and the timesteps

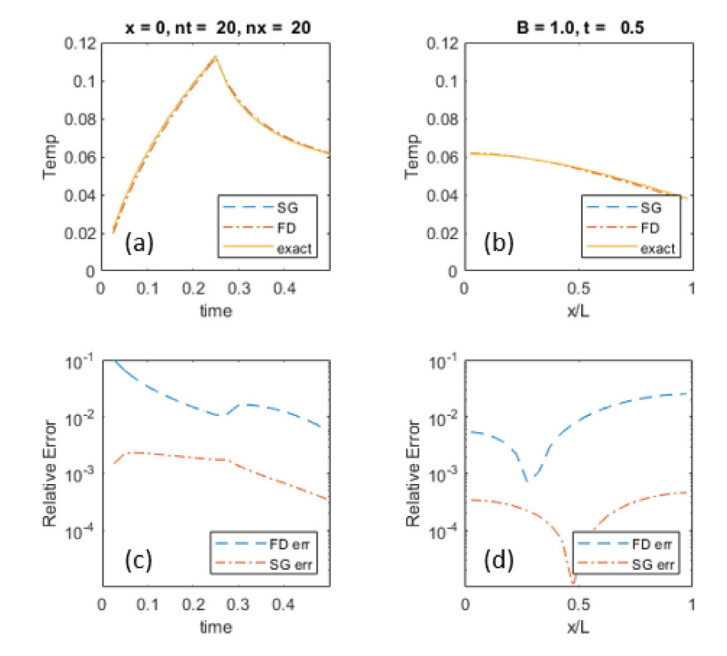


**Fig. 6.** Results for Example 1, case X23B00G(x5t5)T0, for spectral graph (SG), finite difference (FD), and exact solutions. The on-off heating is over spatial region (0 < x/a < 0.25) with heating-off time  $(\tilde{t}_1 = 0.25)$ , under conditions $B_2 = 1.0$ , nt = 20, and nx = 20. (a) Temperature history at the node nearest x = 0, (b) temperature distribution at  $\tilde{t} = 0.5$ , (c) relative error for the temperature history, (d) relative error for the temperature distribution.

are few. The errors for the SG method are smaller than those of FD method by about an order of magnitude, and the errors for both method decrease somewhat over time. The errors for both methods are somewhat larger nearer the boundaries.

The error was also computed from the temperature history at x=0 over the time range  $(0<\tilde{t}<0.5)$ , for several combinations of spatial nodes nx and timesteps nt. For each temperature history the symmetric mean absolute percentage error was computed, defined by

SMAPE = 
$$\frac{1}{nt} \sum_{i=1}^{nt} \frac{|T_{ex}(t_i) - T(t_i)|}{T_{ex}(t_i) + T(t_i)} \times 100\%$$
 (58)

where nt is the number of timesteps,  $T_{\rm ex}(t_i)$  is the exact temperature and  $T(t_i)$  is the numerically computed temperature. The SMAPE results for several temperature histories are listed in Table 2. The errors for the SG method are insensitive to the number of timesteps; recall that the SG method is analytic in time. At nt=20 and Biot =0.1 the SG method has much lower error than the FD method; as nt increases the error for the FD

**Table 2** Symmetric mean absolute percentage error (SMAPE) in SG and FD values for Example 1, case X23B00G(x5t5)T0, versus number of spatial nodes nx and time steps nt. The comparison is made at the node closest to the x=0 boundary over the time range  $(0 < \tilde{t} < 0.5)$ . The body has on-off internal heating over  $(0 < \tilde{x} < 0.25)$  and  $(0 < \tilde{t} \le 0.25)$ .

Biot	nx	nt	SG-SMAPE	FD-SMAPE
0.1	20	20	0.145852	2.639843
		100	0.146105	0.596043
		500	0.145807	0.161724
	40	20	0.036419	2.684466
		100	0.036515	0.632578
		500	0.036437	0.119548
	80	20	0.009102	2.695560
		100	0.009128	0.642124
		500	0.009109	0.128321
10	20	20	0.144412	2.054895
		100	0.144291	0.461525
		500	0.143922	0.125292
	40	20	0.036052	2.112728
		100	0.036055	0.506753
		500	0.035960	0.092108
	80	20	0.009010	2.128024
		100	0.009013	0.520565
		500	0.008989	0.102658

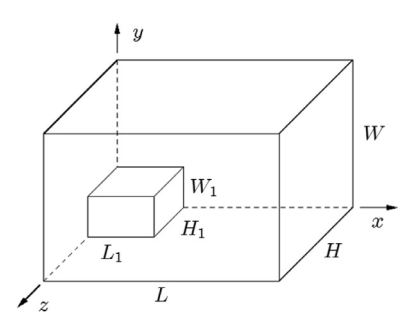


**Fig. 7.** Geometry for the parallelepiped with piecewise initial condition and convection heat loss at the boundaries, case X33B00Y33B00Z33B00T5.

method decreases, becoming comparable with the SG method only at nt = 500. The SG method is sensitive to the number of nodes, improving from about 0.14% error at nx = 20 to 0.009% error at nx = 80 for all values of nt and Biot number listed. In contrast the error for the FD method changes little as nx increases, with no clear trend. All of the errors in Table 2 are small, less than 0.15% for the SG method and less than 2.7% for the FD method.

# 3.2. Example 2. Parallelepiped with piecewise initial condition

The method is applied to a parallelepiped with piecewise initial condition for which an exact analytical solution is available for verification. First the exact solution is given, and then the spectral graph method is applied to nodes distributed in a uniform grid and also with a block-random grid, appropriate for the authors' interest in the thermal modelling of additive manufacturing.

#### 3.2.1. Exact solution in the parallelepiped

Consider heat conduction in a parallelepiped with a piecewise initial condition and with convection heat loss at the boundaries. The geometry is shown in Fig. 7, and this case is denoted X33B00Y33B00Z33B00T5 in the heat conduction numbering system.

The temperature in the parallelepiped satisfies the following energy equation and boundary conditions:

$$\frac{\partial^{2} \tilde{T}}{\partial \tilde{x}^{2}} + \frac{1}{\tilde{W}^{2}} \frac{\partial^{2} \tilde{T}}{\partial \tilde{y}^{2}} + \frac{1}{\tilde{H}^{2}} \frac{\partial^{2} \tilde{T}}{\partial \tilde{z}^{2}} = \frac{\partial \tilde{T}}{\partial \tilde{t}}; \begin{cases} 0 < \tilde{x} < 1\\ 0 < \tilde{y} < 1\\ 0 < \tilde{z} < 1\\ \tilde{t} > 0 \end{cases}$$
(59)

at 
$$\tilde{x} = 0$$
,  $-\frac{\partial \tilde{T}}{\partial \tilde{x}} + B_{x1}\tilde{T} = 0$   
at  $\tilde{x} = 1$ ,  $-\frac{\partial \tilde{T}}{\partial \tilde{x}} - B_{x2}\tilde{T} = 0$   
at  $\tilde{y} = 0$ ,  $-\frac{\partial \tilde{T}}{\partial \tilde{y}} + B_{y1}\tilde{T} = 0$   
at  $\tilde{y} = 1$ ,  $-\frac{\partial \tilde{T}}{\partial \tilde{y}} - B_{y2}\tilde{T} = 0$   
at  $\tilde{z} = 0$ ,  $-\frac{\partial \tilde{T}}{\partial \tilde{z}} + B_{z1}\tilde{T} = 0$   
at  $\tilde{z} = 1$ ,  $-\frac{\partial \tilde{T}}{\partial \tilde{z}} - B_{z2}\tilde{T} = 0$  (60)

$$\tilde{T}(\tilde{x}, \tilde{y}, \tilde{z}, 0) = \begin{cases}
1; & \tilde{x} < \tilde{L}_1; & \tilde{y} < \tilde{W}_1; & \tilde{z} < \tilde{H}_1 \\
0; & \text{otherwise}
\end{cases}$$
(61)

The above problem has been made dimensionless by the following parameters:

$$\tilde{x} = \frac{x}{L}; \quad \tilde{y} = \frac{y}{W}; \quad \tilde{z} = \frac{z}{H}; \quad \tilde{W} = \frac{W}{L}; \quad \tilde{H} = \frac{H}{L}$$

$$\tilde{L}_{1} = \frac{L_{1}}{L}; \quad \tilde{W}_{1} = \frac{W_{1}}{W}; \quad \tilde{H}_{1} = \frac{H_{1}}{H}; \quad \tilde{t} = \frac{\alpha t}{L^{2}}; \quad \tilde{T} = \frac{T}{T_{0}}$$

$$B_{x1} = \frac{h_{x1}L}{k}; \quad B_{x2} = \frac{h_{x2}L}{k}; \quad B_{y1} = \frac{h_{y1}W}{k}; \quad B_{y2} = \frac{h_{y2}W}{k}$$

$$B_{z1} = \frac{h_{z1}H}{k}; \quad B_{z2} = \frac{h_{2}H}{k};$$
(62)

The dimensionless temperature in the parallelepiped is given by:

$$\widetilde{T}(\widetilde{x}, \widetilde{y}, \widetilde{z}, \widetilde{t}) = 8 \left[ \sum_{m=1}^{\infty} \frac{X_m(\widetilde{x}) I X_m}{N_x} e^{-\beta_m^2 \widetilde{t}} \right] \left[ \sum_{n=1}^{\infty} \frac{Y_n(\widetilde{y}) I Y_n}{N_y} e^{-\gamma_n^2 \widetilde{t} / \widetilde{W}^2} \right] \times \left[ \sum_{p=1}^{\infty} \frac{Z_p(\widetilde{y}) I Z_p}{N_z} e^{-\eta_p^2 \widetilde{t} / \widetilde{H}^2} \right]$$
(63)

where

$$X_{m}(\tilde{x}) = \beta_{m} \cos(\beta_{m}\tilde{x}) + B_{x1} \sin(\beta_{m}\tilde{x})$$

$$IX_{m} = \frac{1}{\beta_{m}} \left[ B_{x1} + \beta_{m} \sin(\beta_{m}\tilde{L}_{1}) - B_{x1} \cos(\beta_{m}\tilde{L}_{1}) \right]$$

$$N_{x} = (\beta_{m}^{2} + B_{x1}^{2}) \left[ 1 + \frac{B_{x2}}{\beta_{m}^{2} + B_{x2}^{2}} \right] + B_{x1}$$

$$Y_{n}(\tilde{y}) = \gamma_{n} \cos(\gamma_{n}\tilde{y}) + B_{y1} \sin(\gamma_{n}\tilde{y})$$

$$IY_{n} = \frac{1}{\gamma_{n}} \left[ B_{y1} + \gamma_{n} \sin(\gamma_{n}\tilde{W}_{1}) - B_{y1} \cos(\gamma_{n}\tilde{W}_{1}) \right]$$

$$N_{y} = (\gamma_{n}^{2} + B_{y1}^{2}) \left[ 1 + \frac{B_{y2}}{\gamma_{n}^{2} + B_{y2}^{2}} \right] + B_{y1}$$

$$Z_{p}(\tilde{z}) = \eta_{p} \cos(\eta_{p}\tilde{z}) + B_{z1} \sin(\eta_{p}\tilde{z})$$

$$IZ_{p} = \frac{1}{\eta_{p}} \left[ B_{z1} + \eta_{p} \sin(\eta_{p}\tilde{H}_{1}) - B_{z1} \cos(\eta_{p}\tilde{H}_{1}) \right]$$

$$N_{z} = (\eta_{p}^{2} + B_{z1}^{2}) \left[ 1 + \frac{B_{z2}}{\eta_{p}^{2} + B_{z1}^{2}} \right] + B_{z1}$$
(64)

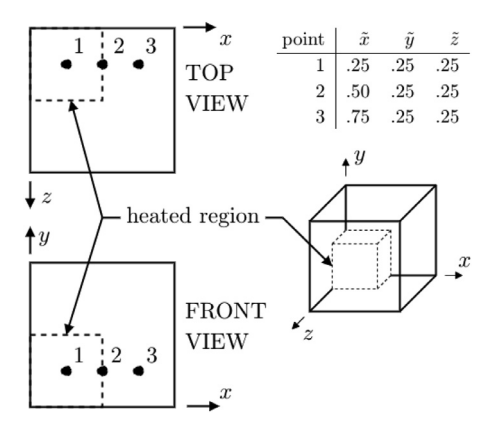


**Fig. 8.** Locations for observing temperature in the parallelepiped: (1) center of heated region; (2) face of heated region; (3) outside heated region. Bodies studied had square cross section (W/L = 1) and varying H/L values.

Eigenvalues  $\beta_m$ ,  $\gamma_n$ , and  $\eta_p$  are roots of the following relations

$$\tan \beta_m = \frac{\beta_m (B_{x1} + B_{x2})}{\beta_m^2 - B_{x1} B_{x2}}; \ \tan \gamma_n = \frac{\gamma_n (B_{y1} + B_{y2})}{\gamma_n^2 - B_{y1} B_{y2}};$$

$$\tan \eta_p = \frac{\eta_p (B_{z1} + B_{z2})}{\eta_p^2 - B_{z1} B_{z2}}$$
(65)

The above series expression converges somewhat slowly when evaluated at small time, but even so ten-digit precision can be obtained for the time ranges needed here. A full discussion of this solution, including a small-time form, tables of numeric values, and computer algorithms, is available elsewhere [47].

#### 3.2.2. Numerical results for uniform rectangular grid

The spectral graph method was carried out for parallelepiped bodies which were initially hot over a small region ( $L_1 = W_1 = H_1 = 0.5$ ). No calibration is needed for the uniform rectangular grid. The temperature was tracked at three points in each body, identified in Fig. 8: (1) at the center of the initially heated region, (2) at an interior face of the initially-heated region, and (3) outside the initially heated region.

First an equal-sided body with L=W=H is studied. The temperature history at the three points is plotted versus time in Fig. 9 for spatially uniform heat transfer coefficient over all surfaces of the cube at levels Bi = 0.1, 1, and 10, and for n/vol = 1728 in a 12x12x12 grid. Location (1) starts at  $\tilde{T}=1$ , location (2) starts at  $\tilde{T}=0.5$ , and location (3) starts at  $\tilde{T}=0.5$  Fig. 9 shows that the SG solution agrees very closely with the exact solution. As the Biot number increases, the temperature at locations (1) and (2) fall more rapidly, and further towards zero. At location (3) the temperature first rises then falls, and for higher Biot number the peak temperature is lower. At large time (not shown) all the temperatures approach zero, and the time it takes to reach zero temperature decreases as the Biot number increases. That is, the cool down is faster at higher heat loss.

Two error measures are used to quantify the agreement between the SG method and the exact solution: the symmetric mean absolution percentage error (SMAPE) defined in Eq. (56) and the root mean square error (RMSE) defined by

$$RMSE = \sqrt{\frac{1}{n_t} \sum_{k=1}^{n_t} \left( T_{SG}^k - T_{EX}^k \right)^2}.$$
 (66)

Table 3 shows the error measures for the SG solution at three locations, at three Biot numbers, over time range  $(0 < \tilde{t} < 0.2)$ , for the equal-sided body L = W = H. Three different node densities are included at n/vol = 512, 1728, and 4096. Table 3 shows that

the SMAPE for n/vol = 1728 (Fig. 9 data) is less than 0.5% and is less than 0.3% for the n/vol = 4096 data. The error values increase slightly as Biot number increases.

The study depicted in Fig. 9 and Table 3 for the equal-sided body was repeated for three other parallelepipeds. Specifically, box-shaped bodies were studied with square cross section W/L = 1but with varying length along the z axis described by H/L = 0.5, 0.75, and 1.5. The initial condition was identical  $(L_1 = W_1 = H_1 =$ 0.5) and the same temperature-observation locations were used (see Fig. 8). The temperature from the SG method for these bodies was compared to the exact solution as before. The temperature plots, omitted for brevity, show close agreement with the exact solution. Table 4 shows the SMAPE and RMSE error values for one body, the parallelepiped W/L = 1 and H/L = 1.5, for three values of the Biot number and for three node densities. Note that the error values are very close in size to those for the equal-sided body (H/L = 1) shown in Table 3. Error values for two additional body shapes H/L = 0.5 and H/L = 0.75 (not shown in the interest of brevity) are also comparable to those in Tables 3 and 4. The point of the discussion is that the SG method can provide high precision temperature values for a variety of body shapes at various levels of surface heat loss, and the level of precision depends strongly on the node density and less strongly on the Biot number.

#### 3.2.3. Numerical results for block-random grid

In this section temperature results are given for the improved spectral graph method carried out on block-random grids on the parallelepiped. The body is divided into equal-sized blocks, and then a fixed number of nodes are placed in each block at random locations. This provides a large-scale uniform node distribution that is small-scale random. This method of node placement is appropriate for thermal simulation of an additive manufacturing process by the spectral graph method, in which the body shape changes as layers (or hatches) are added. The random placement of nodes in each added layer (or hatch) is straightforward and computationally efficient.

Several block-random grids were created for the cube-shaped part by specifying the same number of blocks along each coordinate direction,  $n_b$ , and the number of nodes within each block,  $n_g$ . Table 5 shows the total number of nodes in grids created from different combinations of  $n_b$  and  $n_g$ . For example,  $n_b = 4$  and  $n_g = 3$  give the total number of nodes as  $4 \cdot 4 \cdot 4 \cdot 3 = 192$ . To study the effect of random node locations within blocks, ten grids were created by different random embodiments of each block-grid combination studied, and the results are reported as the mean and variance over these ten grids. The randomly determined points within each block were sampled from a finely divided grid placed on each block, without replacement. In the present work each block was subdivided into  $6^3 = 216$  points.

The calibration procedure for obtaining the gain factor involves a data-fitting procedure between the SG method and the exact solution (refer to Section 2.4.3). The benchmark data for the comparison is the time history of the temperature from the exact solution in the time range (0,0.2) at the center of the initially heated region for a cubic body. This location and this time range was shown to be optimal for calibration through a previous sensitivity study [2]. Twenty temperature values at uniformly-spaced time points were used. The data fitting procedure was the minimization of the sum-of-square error between the exact solution and the SG model carried out with a Gauss-Newton method [48, p. 29]. The method converged to four-digit precision in about six iterations and the resulting gain factor was not sensitive to the initial guess.

The calibration was carried out for several block-random grids at several Biot numbers. Ten block-random grids were studied for each node density so that averages and variance could be found. The resulting average gain factor is plotted in Fig. 10 ver-

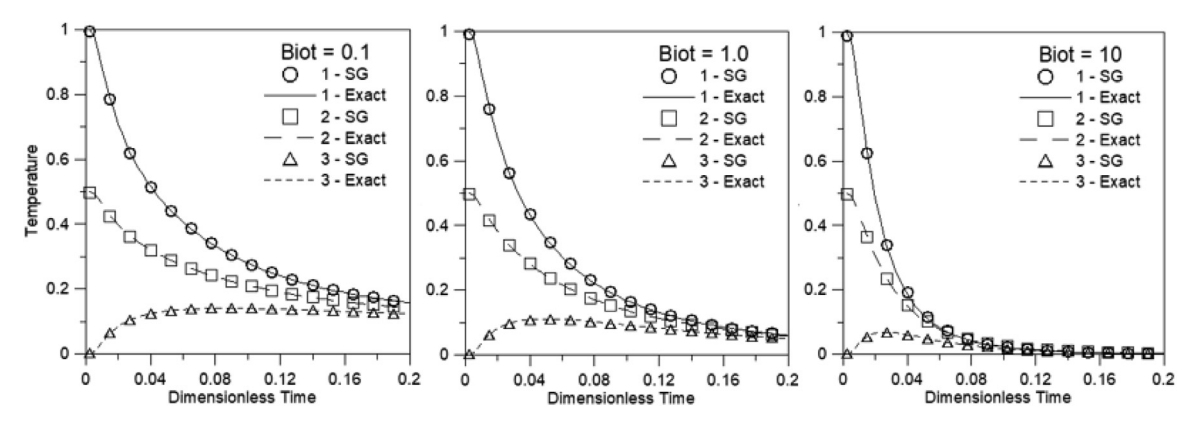


**Fig. 9.** Temperature history at three points in the cube L = W = H (see Fig. 8 for locations) to compare exact and SG solution on a uniform rectangular grid at (a) Biot = 0.1, (b) Biot = 1.0, (c) Biot 10. Parameters for the SG solution are 1536 nodes per unit volume and 80 timesteps.

**Table 3** For the cube with L = W = H with uniform rectangular grid, error (SMAPE and RMSE) for the SG method is compared to exact solution at locations shown in Fig. 8 at three grid densities and three Biot numbers.

			SMAPE			RMSE		
H/L	location	$\frac{\text{nodes}}{\text{vol}}$	Bi=0.1	Bi=1.0	Bi = 10.	Bi=0.1	Bi=1.0	Bi = 10.
1.0	1	512	0.318811	0.448006	0.870092	0.007398	0.010026	0.016782
		1728	0.141872	0.198788	0.386930	0.003398	0.004616	0.008010
		4096	0.079635	0.111562	0.217432	0.001920	0.002617	0.004614
	2	512	0.246750	0.449466	0.563780	0.002870	0.004095	0.006862
		1728	0.109734	0.198981	0.248496	0.001309	0.001865	0.003206
		4096	0.061604	0.111649	0.139236	0.000739	0.001054	0.001833
	3	512	0.670107	0.927687	0.978781	0.001884	0.001936	0.001538
		1728	0.321845	0.435693	0.459108	0.000878	0.000903	0.000728
		4096	0.184793	0.248705	0.261999	0.000497	0.000512	0.000414

**Table 4** For the parallelepiped with (L, W, H) = (1, 1, 1.5), error (SMAPE and RMSE) for the SG method with uniform rectangular grid compared to exact solution at locations shown in Fig. 8 at three grid densities and three Biot numbers.

			SMAPE			RMSE		
H/L	location	$\frac{\text{nodes}}{\text{vol}}$	Bi=0.1	Bi=1.0	Bi = 10.	Bi=0.1	Bi=1.0	Bi = 10.
1.5	1	512	0.314239	0.456059	0.914614	0.007408	0.010030	0.016782
		1728	0.139413	0.202147	0.407239	0.003403	0.004618	0.008010
		4096	0.078168	0.113409	0.228961	0.001922	0.002618	0.004614
	2	512	0.253966	0.454544	0.585879	0.002884	0.004102	0.006862
		1728	0.112648	0.201332	0.259505	0.001315	0.001868	0.003206
		4096	0.063186	0.112990	0.145656	0.000742	0.001056	0.001833
	3	512	0.698852	0.929852	0.955982	0.001898	0.001940	0.001537
		1728	0.334778	0.436741	0.448406	0.000884	0.000905	0.000728
		4096	0.192099	0.249311	0.255869	0.000501	0.000513	0.000414

**Table 5** Number of nodes in a parallelepiped body created by  $n_b$  blocks along each axis and  $n_g$  nodes within each block. Total number of nodes  $= n_b^3 \cdot n_g$ .

	$n_g$							
$n_b$	1	2	3	4	5	6	7	8
4	64	128	192	256	320	384	448	512
6	216	432	648	864	1080	1296	1512	1728
8	512	1024	1536	2048	2560	3072	3584	4096

sus node density (n/vol) and the variances are shown as error bars. Fig. 10 shows that the gain factor resides in a narrow band of values in the range (0.48 - 0.67), and has no clear trend as node density n/vol varies

In examining these values it is important to consider the application to metal additive manufacturing. In cooling of metal the Biot number is usually small. For example, for a large stainless steel part (L = 15 cm and  $k \approx 20$  W/m/K) exposed to a large heat transfer coefficient (h=100 W/m²/K), the Biot number is Bi =  $100 \cdot 0.15/20 = 0.75$ . Other metals with higher thermal conductivity give even lower values of the Biot number. This suggests that the gain values in Fig. 10 should be examined for Bi  $\leq 1.0$  values. For these smaller Biot values, the gain values lie in the range (0.58 - 0.67), a range of 14%, and the variation is smaller as the node density increases. This suggests that the gain is independent of the Biot number, so that one calibration is sufficient to characterize the spectral graph method for the range of Biot numbers found in metal additive manufacturing.

Figure 11 shows temperature versus time for the SG method on a single block-random grid with node density 1536 (nodes per unit volume) compared to the exact solution at three locations and for three Biot numbers, The results agree very closely at location 1, the center of the heated region, because this location was used to fit the gain factor f. The agreement is also good at location 3

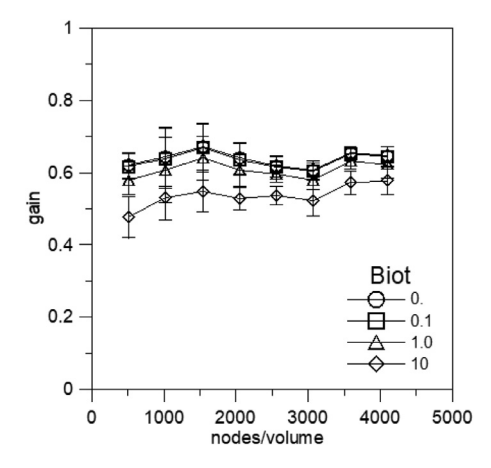


**Fig. 10.** Average gain versus node density (n/vol) at several Biot numbers. For each node density n/vol, ten block-random grids were used to find averages; error bars show the variance.

(unheated region). At location 2 the SG method slightly overestimates the temperature at early time and slightly underestimates the temperature at middle time. The long time temperature trends are correct at all locations.

As before, a quantitative measure of the error in the SG method for the block-random grid is provided by SMAPE defined in Eq. (58) and RSME defined in Eq. (66) as shown in Table 6. Table 6 shows error values for the block-random grid at three locations, three Biot numbers, and three grid densities. To address the issue of randomness in assigning node locations, ten different block-random grids were created for each node density to obtain the averages and variances reported in Table 6.

Table 6 shows that the SMAPE error for n/vol = 1536 is everywhere less than 10% and less than 6% for n/vol = 4096, with the highest value for Biot = 10 (high cooling rate). The RMSE errors are included because SMAPE errors skew large at large Biot number, because of division by very small temperature values at later times. The RMSE values for n/vol = 1536 are everywhere less than 0.019 and less than 0.014 for n/vol = 4096. No exploration of the number of time steps is included here; error in the spectral graph method varies little with the number of time steps, which was evident earlier in Table 2 for the one-dimensional example. Recall that the SG method is analytic in time, as discussed in Section 2.5.

Earlier the Biot number was identified to be in the range Bi  $\leq 1.0$  for metal additive manufacturing. For this limited range of Biot values, the SMAPE errors in Table 6 for n/vol = 1536 are everywhere less than 6% and are less than 3% for n/vol = 4096.

# 4. Validation with experimental data from additive manufacturing

Validation of the improved spectral graph method was carried out by comparison with experimental temperatures from infrared camera data obtained during a test build with the laser powder bed fusion (LPBF) process.

# 4.1. Experimental setup

The additive manufacturing build was created on an open architecture LPBF system at Edison Welding Institute, Columbus, Ohio. A long wave infrared (LWIR) thermal camera was placed offaxis with an angle about 80° to the horizontal. A representative schematic along with an image of the experimental setup in shown in Fig. 12. The Micro Epsilon model TIM-640 LWIR thermal camera used in the experiment has a resolution of 640 by 480 pixels. At the camera's height, the spatial resolution of the build plate was approximately 20 pixels per mm². The camera was calibrated according to a black-body technique detailed in previous work [4]. This calibration technique enabled the thermal camera to accurately measure top surface temperatures up to 550 °C.

The parts in the experiment were made from the Inconel 718 powder. Seventeen parts were created from six different geometries, each with a different purpose. Part distortion, recoater crash and powder feed failures were investigated in a previous work by [5] using several geometries in this build. For the purposes of this work, data from two inverted half cones were studied with base height 6 mm, base radius 4 mm, and part height 20 mm. These two geometries as well as the completed build plate containing these parts are shown in Fig. 13.

These two geometries with overhang were selected as they were expected to experience significant overheating, which can lead to superelevation and build failure in LPBF. For this reason, rapid prediction of the thermal history is of interest.

# 4.2. Experimental end-of-cycle temperature

The procedure for obtaining the end-of-cycle surface temperature from the thermal images is described for the cone-shaped part with  $45^{\circ}$  inclination angle (C45). For C45, a 9 pixel by 9 pixel region from the IR camera data was selected. This sampled area is annotated in Fig. 14(a) and equates to a  $4~{\rm mm}^2$  area on the top surface of the part. Measurement near the edge of the part was avoided as the blur from the thermal image would lead to measurement error. Temperature readings from the infrared thermal camera image from this  $4~{\rm mm}^2$  area were averaged to obtain a top surface temperature. The temperature trend for this sampled

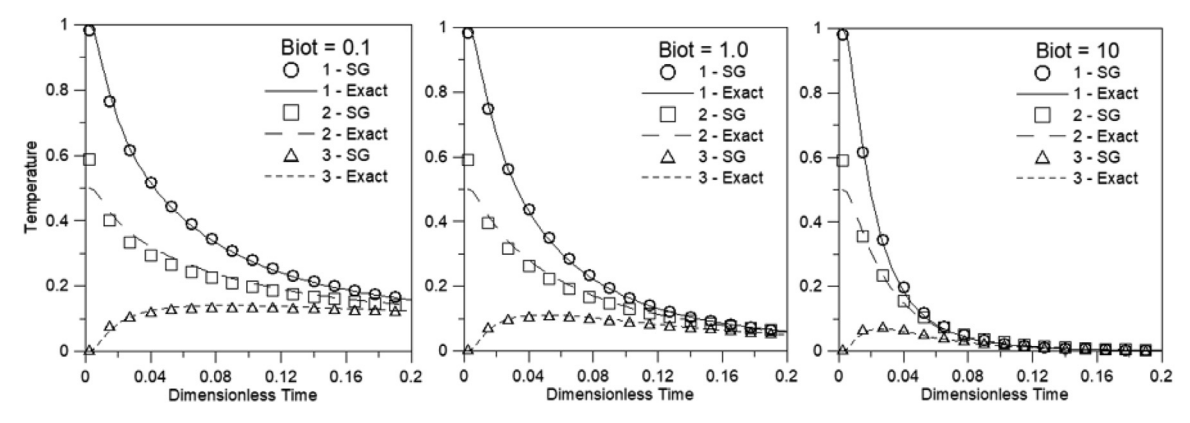


**Fig. 11.** Temperature history at three points in the cube (see Fig. 8 for locations) to compare exact and SG solutions at (a) Biot = 0.1, (b) Biot = 1.0, (c) Biot = 10. Parameters for the SG solution are 1536 nodes on a block-random grid and 80 timesteps.

**Table 6** Error in temperature for the SG method on the block-random grid at three locations defined in Fig. 8 and for three Biot numbers. For each grid density n/vol, ten block-random grids were studied to obtain averages and variances over time range  $(0 < \tilde{t} < 0.2)$ .

	Bi		SMAPE		RMSE		
Location		n	average	variance	average	variance	
1	0.1	512	1.876834	0.331491	0.01719120	0.00001359	
		1536	0.940356	0.156959	0.00992803	0.00000993	
		4096	0.935124	0.234455	0.00887210	0.00001160	
	1	512	2.753140	0.660255	0.01666274	0.00000743	
		1536	1.520414	0.395436	0.01001318	0.00000968	
		4096	1.090323	0.276723	0.00785373	0.00000529	
	10	512	6.598844	7.072547	0.01498143	0.00000495	
		1536	5.905686	10.858103	0.01013748	0.00000395	
		4096	3.859102	3.502287	0.00782939	0.00000339	
2	0.1	512	2.190329	1.210556	0.01494754	0.00006074	
		1536	2.393353	2.395105	0.01890678	0.00011668	
		4096	2.030881	1.911114	0.01358837	0.00007339	
	1	512	1.866639	0.454295	0.01264575	0.00005338	
		1536	2.829961	2.987142	0.01816824	0.00012125	
		4096	1.944417	2.135573	0.01215211	0.00006857	
	10	512	5.921486	12.519991	0.01069555	0.00005730	
		1536	8.302355	28.161460	0.01847190	0.00022798	
		4096	4.754935	9.625067	0.01063742	0.00003648	
3	0.1	512	4.632983	4.616591	0.01179445	0.00002433	
		1536	4.022486	3.960269	0.01011096	0.00002245	
		4096	2.179375	1.051766	0.00550174	0.00000649	
	1	512	5.234295	5.352751	0.01009804	0.00001224	
		1536	5.128025	6.565621	0.00960630	0.00002222	
		4096	2.755790	0.987612	0.00549648	0.00000388	
	10	512	9.902535	33.144596	0.00645721	0.00000949	
		1536	9.050974	17.936956	0.00720693	0.00001416	
		4096	5.492360	3.038816	0.00443783	0.00000254	

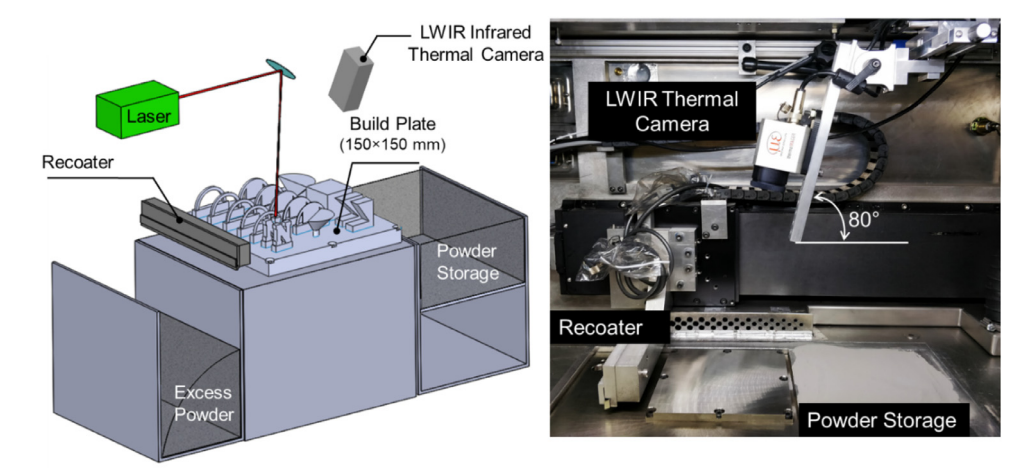


Fig. 12. (Left) Schematic of open architecture LPBF platform and the LWIR camera setup. (Right) Photograph of the build setup used in the experiment.

region over the entire build duration of C45 is shown in Fig. 14(b). The cone-shaped parts were completed at layer 500, the entire build completed at layer 650. A sample of the temperature trend over three layers is shown in Fig. 14(c).

From the raw temperature data shown in Fig. 14(b), the end-of-cycle surface temperature was extracted in the following manner. Referring to Fig. 14(c), the raw temperature has three prominent features, demarcated (A), (B), and (C), which correspond to specific process events. Note that the thermal camera acquires data only when the laser is active through a triggering mechanism. The first large spike marked (A) is when the laser is striking the sampled 4 mm<sup>2</sup> pixel region. The temperature recorded at (B) is momentarily interrupted at the time the laser and camera are both switched off. The epoch marked (C) and beyond is for the next layer processed by the laser. In the interim between (B) and (C) the recoater fetches powder, and a fresh powder layer is deposited.

The time for recoating is measured to be 11 seconds, and remains fixed irrespective of the process conditions or number of parts on the build plate. The temperature in the instant just before the laser strikes the sampled area again, before the melting of a new layer, is termed as the end-of-cycle surface temperature. Plotted in Fig. 14(d) is the end-of-cycle surface temperature for the 9 pixel by 9 pixel area (4 mm²) of the cone-shaped part C45 sampled in Fig. 14(a). More information on the experimental set up and on the reduction of the LWIR data is available elsewhere [5].

#### 4.3. Assumptions in the thermal model

There are several simplifying assumptions applied to both SG and FE methods for thermal modeling of the LPBF process. Because the duration of laser scan on one part (less than 0.5 s) is much shorter than interlayer time (> 30 s), the laser scan is mod-

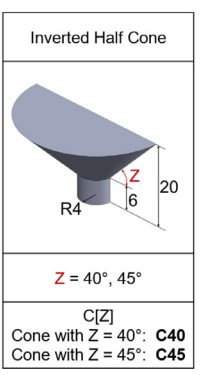




**Fig. 13.** (Left) Inverted half cone geometry used to validate this work. Two similar geometries were created, one with overhang angle 40 degrees and one with 45 degrees. (Right) Completed build plate with the two inverted half cones (C40, C45) used in this work. Other parts on this build plate were used for a different research topic.

eled as the instantaneous appearance of a newly fused layer. Latent heat effects of melting and fusing are neglected. The thermal model is carried out on a succession of heating cycles, with each cycle starting with the addition of the newly-fused layer and continuing to the end-of-cycle condition before the next laser scan. The interlayer time, which can vary throughout the build depending on the area to be fused at each layer, was obtained directly from the G-code, the machine language which encodes the processing parameters to carry out the actual build. The end-of-cycle temperature from one cycle is the initial condition for the body in the subsequent heating cycle, except for the newly-fused surface layer which increases the size of the computational domain. In the present embodiment of the SG method, the energy added by the laser is modeled as a temperature jump above the previous layer's end-of-cycle temperature. The temperature jump is determined at the first layer as  $\Delta T = T_{melt} - T_{ambient} = 1600 C - 250 C$  in the present example. In this way the same energy per unit volume is added to each newly fused layer. Refer to [2] for further discussion of these assumptions.

#### 4.4. Calibration

Every numerical method contains parameters that must be chosen so that the results are physically meaningful. For the SG method, calibration is needed to find the gain factor using the method described in Section 3.2.3. The analytical solution described in Section 3.2.1 was used to compute a single heating/cooling cycle in an Inconel 718 parallelepiped depicted in Fig. 8 with each side of length 25 mm. The spectral graph method was applied to this geometry, and the gain factor was chosen to provide the best fit between the analytical solution and the spectral graph model. The comparison was carried out at the center of the initially-heated region. In this way the gain factor of f=0.555 was chosen at which the SMAPE was 0.4%. This gain factor was used for all subsequent model calculations. Other parameters used in the calibration are given in Table 7.

Another calibration step is to determine the correct level of heat loss for the simulation. To do this, the SG model was applied to inverted-cone geometry C40, with the larger overhang, and end-of-cycle temperatures were compared to data from the experimental build. The model was run with 50 superlayers, that is, 50 heating cycles in succession to represent the actual 500 layers in the build. The build plate on which the part is built, the primary heat sink in the problem, was modeled as a large convection coefficient (also called a contact conductance). The value of  $h_b = \frac{1}{2} \frac{1}{2}$ 

**Table 7**Summary of simulation of parameters used for the gain factor calibration and inverted half cone simulations.

Parameters, calibration on parallelepiped	Values
Parallelepiped side length [mm]	25
Specific Heat [J kg <sup>-1</sup> K <sup>-1</sup> ]	435
Conductivity [Wm <sup>-1</sup> K <sup>-1</sup> ]	19.47
Density, [kg m <sup>-3</sup> ]	8,193
Melting Point [C]	1,600
Ambient chamber temperature, [C]	250
Gain factor	0.555
Parameters, simulation of inverted half cones	Values
Radius factor $(\epsilon)$	$\sqrt{2}$
Convection coeff. for powder, $h_w$ [Wm <sup>-2</sup> K <sup>-1</sup> ]	2.5
Convection coeff. for build plate, $h_b$ [Wm <sup>-2</sup> K <sup>-1</sup> ]	300
Superlayer thickness [mm]	0.4 (10 actual layers)
Node density [nodes mm <sup>-3</sup> ]	1.0
Computer hardware	Ryzen 3970X CPU
	3.70 GHz, 128 GB RAM.

**Table 8**Results of convergence study on node density applied to inverted half cone C40.
Density 1.0 node/mm³ was selected to balance decreases in model error against increases in computation time.

Node Density (node/mm³)	Number of nodes	Time (sec)	SMAPE (%)	RMSE (°C)
0.3	1678	2.6	4.06	46.7
0.5	2804	5.1	2.68	32.7
0.8	4478	12.6	2.66	30.1
1	5565	19.3	2.64	29.3
1.5	8256	43.7	2.09	21.7
2	11094	90.3	2.04	21.0

300 W/(m<sup>2</sup>K) was chosen for the build plate; this value is sufficiently large to represent a fixed-temperature boundary condition, because larger  $h_h$  values give the same result. The effect of heat loss to the surrounding powder was modeled as another convection coefficient, to describe the heat loss to the low-conductivity metal powder on the sides of the fused part, and heat loss to the gas at the exposed upper surface of the fused part. To choose the heat-loss coefficient, the error (SMAPE) between the SG model for the C40 part and the end-of-cycle temperature obtained from the LWIR thermal camera was minimized. In this way the value of  $h_w = 2.5$  [W m<sup>-2</sup> K<sup>-1</sup>] was chosen; other parameters for the 50-layer simulation are provided in Table 7. The SG model for the calibration case is shown in Fig. 15a. The dashed line shows the ensemble average of 10 computer runs using 10 different blockrandom grids and the shaded region shows the variance of the 10 different grids. The average error is less than 3% SMAPE and 30 °C RMSE.

A convergence study was also carried out on the node density for the 50-layer simulation of the C40 part. Fig. 16 shows some of the results from this study compared to experimental data for the end-of-cycle temperature. A list of SMAPE error values from the temperature histories in the convergence study, along with computation time for each simulation, is given in Table 8. Table 8 shows that the chosen node density of 1.0 node/mm³ provides a good balance between rapid computation and acceptable precision.

#### 4.5. Results for test case

Using the simulation parameters from calibration procedure, the simulation was carried out for the C45 geometry, with the smaller overhang. The results of the comparison between the SG model and the experimental data is presented in Fig. 15b. The trends are correct and the general shape of the temperature is correct, with the error in the SG model prediction for the C45 part (test case) less than 5% SMAPE and 41 ° C RMSE. The run time for

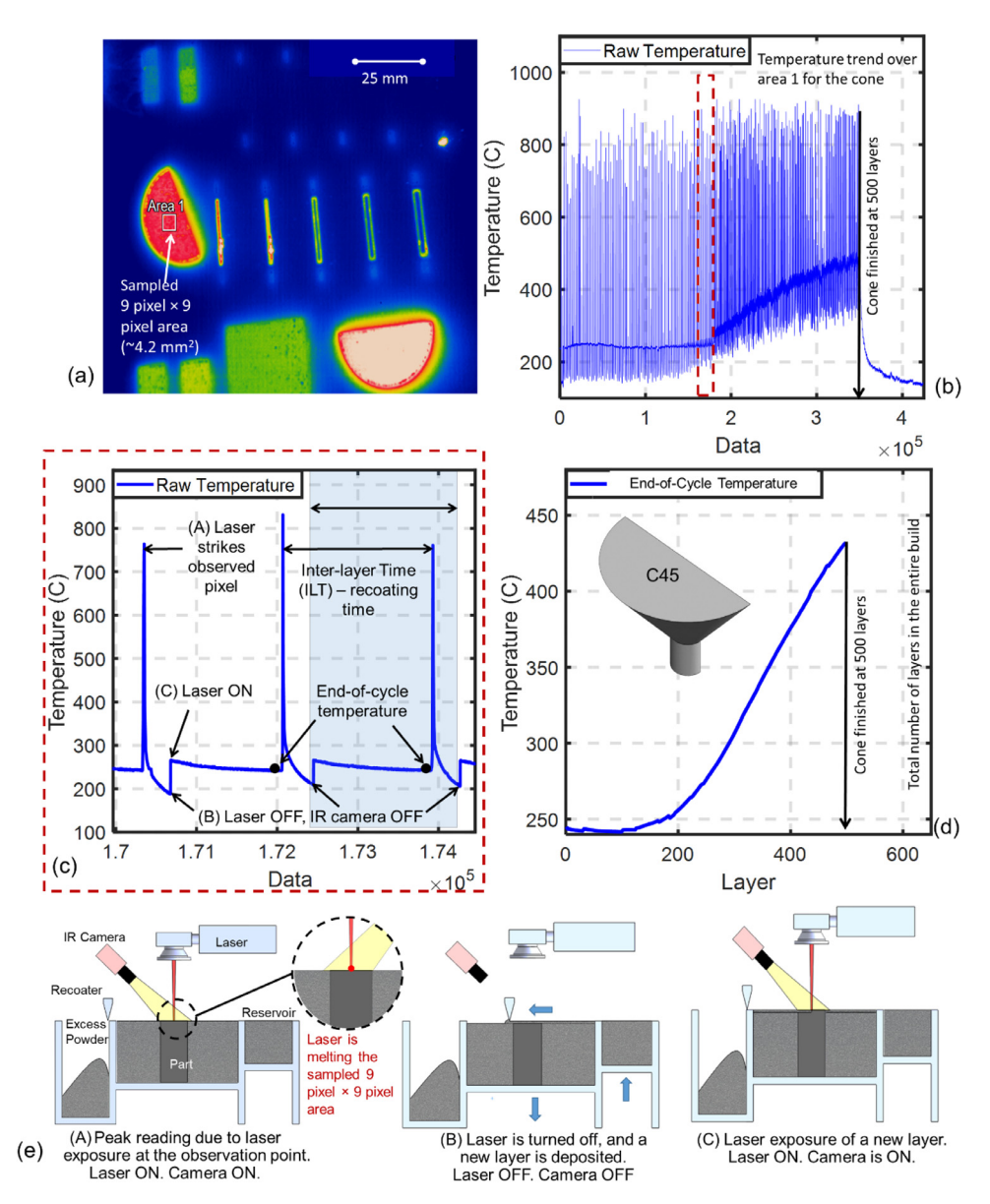


**Fig. 14.** (a) IR image showing the 9 pixel by 9 pixel area over which the surface temperature trends are averaged for the C45 cone-shaped test artifact. (b) The surface temperature trends for the entire duration of the build. (c) The zoomed in area of the temperature trends over three process cycles, including the where the end-of-cycle temperature is obtained. There are three prominent epochs that are observed in the temperature trends on account of process events, labeled (A) through (C) (d) the end-of-cycle surface temperature for the duration of build corresponding to C45. (e) The process events that cause the three epochs observed in the temperature trends in (c).

the C45 test part is smaller than for the C40 calibration part because the smaller part volume contains fewer nodes at fixed node density.

The simulation for the C45 test case somewhat overestimates the end-of-cycle temperature in the overhang region of the part. This mismatch is primarily a function of the overall energy budget in each heating cycle, that is, heat in minus heat out. Evidence for this is the large Fourier number associated with one heating cycle, specifically, Fo =  $\alpha t/L^2 = 0.55$  for  $\alpha = 5.46(10)^{-6}$  m²/s (Inconel), t = 40 s (interlayer time at end of build) and L = 20 mm (height at end of build). At this Fourier number the spatial details of the initial temperature are long forgotten and the temperature distribution is quasi-steady in space and decaying in time. To address the energy budget, areas for future work include improving heat addition in the simulation to more closely agree with the physics of laser absorption, and, improving heat loss to the surroundings, for example by including radiation heat loss.

# 5. Summary and discussion

The SG method has been extended to directly incorporate heat loss with a generalized boundary condition, which is a distinct improvement over the ad hoc heat loss method used previously. Improved edge weights in the Laplacian matrix are now based on the physics of the problem, which reduces the number of calibration parameters and consequently simplifies the calibration process. The improved SG method has been used to develop a discrete Green's function for comprehensive treatment of several heating effects: space-varying initial conditions; time-and-space varying boundary heating; and, time-and-space varying internal heating. The precision of the method was determined from one-dimensional and three dimensional benchmark examples for which exact solutions were available. The one-dimensional example was also compared with a finite difference solution. The method was also applied to a 50-layer simulation of an additive manufacturing

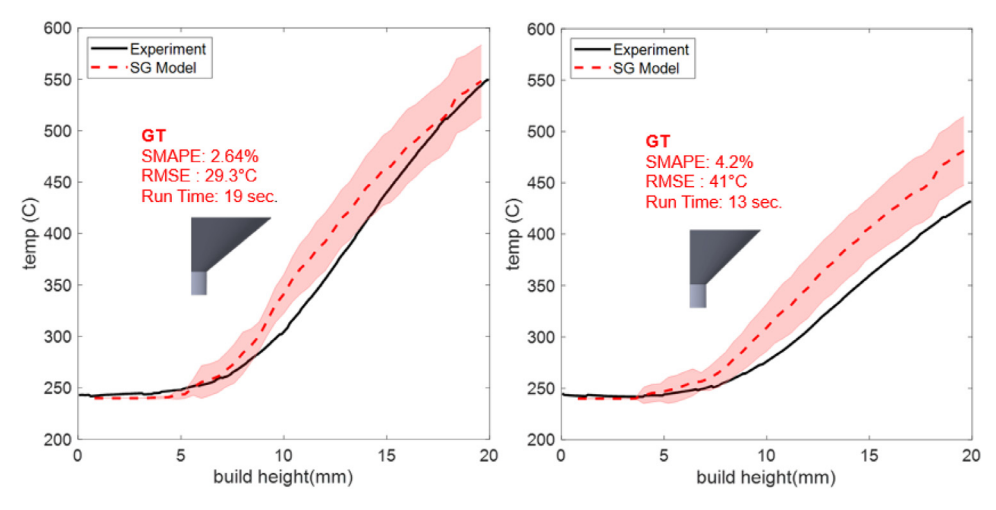
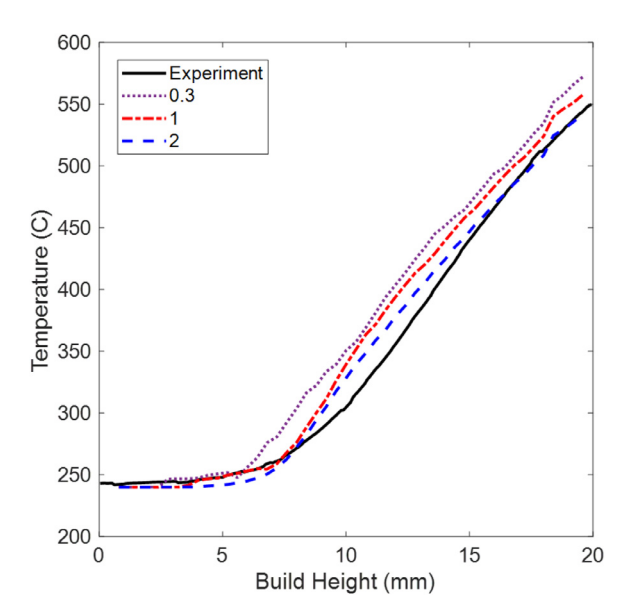


Fig. 15. End-of-cycle temperature histories for the inverted half cones. The dashed red lines are the ensemble average SG model values and the shaded region show the variance from ten block-random grids. The solid black lines are the experimentally measured values for each geometry. (a) The C40 data was used to calibrate the part-to-powder convection coefficient of the model, and (b) the C45 data served as the test case. (For interpretation of the references to colour in this figure legend, the reader is referred to the web version of this article.)



**Fig. 16.** Convergence study on node density for a 50-layer simulated build of the C40 inverted half cone, compared to experimental data. Model results are shown for node density of 0.3, 1.0, and 2.0 nodes/mm<sup>3</sup> and fixed gain factor f = 0.555.

process for two bodies with severe overhang, and the simulation results were validated by comparison with experimental temperature measurements. The model agrees with the experiments within 5% SMAPE with model computation time of less than one minute on a desktop computer. The rapid computation time of this improved thermal model provides an opportunity for application to flaw detection using real-time thermal sensor data; this is an area of ongoing research [49].

The computational advantage of the SG method applied to additive manufacturing comes from a combination of low-cost grid generation, only one eigenvalue solution to find the GF, and analytic behavior on time which allows for time steps of any size. In contrast the finite element (FE) method has high-cost mesh generation and numerical time-integration with many small time steps required to control precision. The computational advantage of the SG method is strong for the rough and rapid thermal simulations that are presently sufficient to advance the field of thermal modeling of 3D printing. However, the computational cost of

the eigenvalue problem in the SG method scales as  $O(n^3)$ , compared to the computational cost of the FE method which scales as  $O(m \cdot n^2)$  where n is the number of nodes and m is the number of timesteps [50]. This suggests that the computational advantage of the SG method may wane when n is large, for example, in simulation of large bodies. To address this concern, work is in progress to develop techniques for SG simulation of large bodies, to limit the number of nodes while maintaining acceptable precision [51].

# **Credit Author Statement**

The material in the above manuscript is original and has not been submitted for publication elsewhere. The work described therein was carried out at our University under funding from the US National Science Foundation.

#### **Declaration of Competing Interest**

Regarding the above paper, I certify that the authors have no conflicts of interest related to publication of our work.

#### Acknowledgement

The authors acknowledge funding from the Department of Energy (DOE) [grant number DE-SC0021136] and the National Science Foundation (NSF) [grant numbers CMMI-1719388, CMMI-1920245, CMMI-1739696, CMMI-1752069, PFI-TT 2044710] under program officers Salim Iqbal, Kevin Chou, Prakash Balan, and Martha Dodson. Thanks are also extended to Reza Yavari for sharing data obtained during an NSF-funded internship at Edison Welding Institute, Columbus, Ohio.

### References

- M.R. Yavari, K.D. Cole, P.K. Rao, Thermal modeling in metal additive manufacturing using graph theory,' ASME transactions, J. Manuf. Sci. Eng. 141 (7) (2019) 071007–071027. doi:10.1115/1.4043648.
- [2] K.D. Cole, M.R. Yavari, P.K. Rao, Computational heat transfer with spectral graph theory: quantitative verification, Int. J. Thermal Sciences 153 (2020) 106383. doi:10.1016/j.iithermalsci.2020.106383.
- [3] A. Gaikwad, M.R. Yavari, M. Montazeri, K.D. Cole, L.K. Bian, P.K. Rao, To-ward the digital twin of additive manufacturing: integrating thermal simulations, sensing, and analytics to detect process faults, IISE Transactions (2020), doi:10.1080/24725854.2019.1701753.
- [4] R. Yavari, R.J. Williams, K.D. Cole, P.A. Hooper, P.K. Rao, Thermal modeling in metal additive manufacturing using graph theory: experimental validation

- with in-situ infrared thermography data from laser powder bed fusion, ASME. J. Manuf. Sci. Eng. (2020), doi:10.1115/1.4047619.
- [5] R. Yavari, Z. Smoqi, B. Bevans, H. Kobir, H. Mendoza, H. Song, K.D. Cole, P.K. Rao, Part-scale thermal simulation of laser powder bed fusion using graph theory: effect of thermal history on porosity, microstructure, and recoater-crash, Mater. Des. 204109685. doi:10.1016/j.matdes.2021.109685.
- [6] F. de Monte, J.V. Beck, D.E. Amos, A heat-flux based "building block" approach for solving heat conduction problems, Int. J. Heat Mass Transfer 54 (13–14) (2011) 2789–2800.
- [7] K.D. Cole, J.V. Beck, A. Haji-Sheikh, B. Litkouhi, Heat Conduction Using Green's Functions, 2nd edition, CRC Press, New York, 2011.
- [8] Y.C. Zhang, M. Blattner, Y.K. Yu, Heat conduction process on community networks as a recommendation model, Phys. Rev. Lett. 99 (15) (2007), doi:10. 1103/PhysRevLett.99.154301.
- [9] J. Ma, W.M. Huang, S. Segarra, A. Ribeiro, Diffusion filtering of graph signals and its use in recommended systems, in: 41st Int. Conf. on Acoustics, Speech and Signal Processing, Shanghai, China, 20–25 March 2016, 2016, 2016, doi:10. 1109/ICASSP.2016.7472541.
- [10] R. Zhang, E.R. Hancock, Graph spectral image smoothing using the heat kernel, Pattern Recognit 41 (2008) 3328–3342.
- [11] J. Solomon, PDE approaches to graph analysis, 2015. arXiv:1505.00185.
- [12] E. Bendito, A. Carmona, A.M. Encinas, Solving dirichlet and poisson problems on graphs by means of equilibrium measures, Europan J. Combinatorics 24 (4) (2003) 365–375.
- [13] A.C. Gilbert, J.G. Hoskins, J.C. Schotland, Diffuse scattering on graphs, Linear Algebra Appl 496 (2016) 1–35.
- [14] C. Arauz, A. Carmona, A.M. Encinas, M. Mitjana, Green functions on product networks, Discrete Appl. Math. 263 (2019) 22–34, doi:10.1016/j.dam.2018.10. 004.
- [15] V.K. Tewary, E.J. Garboczi, Semi-discrete green's function for solution of anisotropic thermal/electrostatic boussinesq and mindlin problems: application to two-dimensional material systems, Eng Anal Bound Elem 110 (2019) 56-68.
- [16] S.Y. Chung, Y.S. Chung, J. Kim, Diffusion and elastic equations on networks, Research Insit. Mathematical Sciences 43 (3) (2007) 699–726.
- [17] H. Xu, S.T. Yau, Discrete green's functions and random walks on graphs, J. Combinatorial Theory Series A 120 (2) (2013) 483–499.
- [18] W.J. Mansur, C.A.B. Vasconcellos, N.J.M. Zambrozuski, O.C. Rotunno Filho, Numerical solution for the linear transient heat conduction equation using an explicit green's approach, Int. J. Heat Mass Transfer 52 (2009) 694–701.
- [19] F.S. Loureiro, W.J. Mansur, A new family of time integration methods for heat conduction problems using numerical green's functions, Comput Mech 44 (4) (2009) 519–531.
- [20] F.S. Loureiro, W.J. Mansur, C.A.B. Vasconcellos, A hybrid time/laplace integration method based on numerical green's functions in conduction heat transfer, Computer Methods in Applied Mecahnics and Engineering 198 (33–36) (2009) 2662–2672.
- [21] Y. Zhang, X. Li, Heat transfer formalism using GFM and FEM in underground tunnels, Build Environ 143 (2018) 717–726.
- [22] V. Sodan, S. Stoffels, H. Oprins, Fast and distributed thermal model for thermal modeling of gan power devices, IEEE Transactions on Components Packaging and Manufacturing Technology 8 (10) (2018) 1747–1755.
- [23] Y.A. Melnikov, V. Reshniak, A semi-analytical approach to green's functions for heat equation in regions of irregular shape, Eng Anal Bound Elem 46 (2014) 108–115.
- [24] W. Mai, S. Soghrati, R.G. Buchheit, A green's discrete transformation meshfree method for simulating transient diffusion problems, Int. J. Numer. Meth. Engng (2016), doi:10.1002/nme.5226.
- [25] L.J. Wang, J.F. Xu, J.X. Wang, The green's functions for peridynamic non-local diffusion, Proceedings of the Royal Society: Mathematical, Physical and Engineering Sciences 472 (2193) (2016) 1–15. https://www.jstor.org/stable/26159822
- [26] J.K. Eaton, The discrete green's function for convective heat transfer part 1: definition and physical understanding, J. Heat Transfer 142 (10) (2020) 102101.
- [27] M. Montazeri, R. Yavari, P. Rao, P. Boulware, In-process monitoring of material cross-contamination defects in laser powder bed fusion, J. Manuf. Sci. Eng. 140 (11) (2018) 111001–111001-111019, doi:10.1115/1.4040543.
- [28] J.C. Fox, S.P. Moylan, B.M. Lane, Effect of process parameters on the surface roughness of overhanging structures in laser powder bed fusion additive manufacturing, Procedia CIRP 45 (2016) 131–134, doi:10.1016/j.procir.2016.02.347.
- [29] G. Strano, L. Hao, R. Everson, K. Evans, A new approach to the design and optimisation of support structures in additive manufacturing, The International Journal of Advanced Manufacturing Technology 66 (9–12) (2013) 1247–1254, doi:10.1007/s00170-012-4403-x.
- [30] D. Thomas, The Development of Design Rules for Selective Laser Melting, Ph.D. dissertation, University of Wales, 2009.

- [31] M. Jamshidinia, R. Kovacevic, The influence of heat accumulation on the surface roughness in powder-bed additive manufacturing, Surf. Topogr. Metrol. Prop. 3 (1) (2015) 014003, doi:10.1088/2051-672X/3/1/014003.
- [32] E.R. Denlinger, J. Irwin, P. Michaleris, Thermomechanical modeling of additive manufacturing large parts, J. Manuf. Sci. Eng. 136 (6) (2014) 061007-061007-061008. doi:10.1115/1.4028669.
- [33] T. DebRoy, H.L. Wei, J.S. Zuback, T. Mukherjee, J.W. Elmer, J.O. Milewski, A.M. Beese, A. Wilson-Heid, A. De, W. Zhang, Additive manufacturing of metallic components – process, structure and properties, Prog Mater Sci 92 (2018) 112–224. doi:10.1016/j.pmatsci.2017.10.001.
- [34] P. Foteinopoulos, A. Papacharalampopoulos, P. Stavropoulos, On thermal modeling of additive manufacturing processes, CIRP J. Manuf. Sci. Technol. 20 (2018) 66–83, doi:10.1016/j.cirpj.2017.09.007.
- [35] A. Bandyopadhyay, K.D. Traxel, Invited review article: metal-additive manufacturing-modeling strategies for application-optimized designs, Addit. Manuf. (2018), doi:10.1016/j.addma.2018.06.024.
- [36] E.R. Denlinger, M. Gouge, P. Michaleris, Thermo-mechanical Modeling of Additive Manufacturing, Butterworth-Heinemann, 2018.
- [37] M.M. Francois, A. Sun, W.E. King, N.J. Henson, D. Tourret, C.A. Bronkhorst, N.N. Carlson, C.K. Newman, T. Haut, J. Bakosi, J.W. Gibbs, V. Livescu, S.A. Vander Wiel, A.J. Clarke, M.W. Schraad, T. Blacker, H. Lim, T. Rodgers, S. Owen, F. Abdeljawad, J. Madison, A.T. Anderson, J.L. Fattebert, R.M. Ferencz, N.E. Hodge, S.A. Khairallah, O. Walton, Modeling of additive manufacturing processes for metals: challenges and opportunities, Curr. Opin. Solid State Mater. Sci. 21 (4) (2017) 198–206, doi:10.1016/j.cossms.2016.12.001.
- [38] B. Cheng, S. Shrestha, Y.K. Chou, Stress and deformation evaluations of scanning strategy effect in selective laser melting, Proc. ASME 2016 11th International Manufacturing Science and Engineering Conference, American Society of Mechanical Engineers.
- [39] R.J. Williams, C.M. Davies, P.A. Hooper, A pragmatic part scale model for residual stress and distortion prediction in powder bed fusion, Addit. Manuf. (2018), doi:10.1016/j.addma.2018.05.038.
- [40] K. Zeng, D. Pal, H.J. Gong, N. Patil, B. Stucker, Comparison of 3DSIM thermal modelling of selective laser melting using new dynamic meshing method to ANSYS, Mater. Sci. Technol. 31 (8) (2015) 945–956, doi:10.1179/1743284714Y. 0000000703.
- [41] N. Peter, Z. Pitts, S. Thompson, A. Saharan, Benchmarking build simulation software for laser powder bed fusion of metals, Addit. Manuf. 36 (2020) 101531, doi:10.1016/j.addma.2020.101531.
- [42] R.L. McMasters, F. de Monte, J.V. Beck, Generalized solution for twodimensional transient heat conduction problems with partial heating near a corner, J. Heat Transfer 141 (7) (2019) 071301, doi:10.1115/1.4043568.
- [43] S.V. Patankar, Numerical Heat Transfer and Fluid Flow, Hemisphere Publishing Corporation, New York, 1980.
- [44] C. Pozrikidis, An introduction to Grids, Graphs, and Networks, Oxford University Press, Oxford, UK, 2014, p. 284.
- [45] B. Çetin, Y.F. Kuşcua, B. Çetin, O. Tümüklüd, K.D. Cole, Semi-analytical source (SAS) method for 3-d transient heat conduction problems with moving heat source of arbitrary shape, Int. J. Heat Mass Transfer (2020), doi:10.1016/j. ijheatmasstransfer.2020.120692.
- [46] Å. Hassebrook, R. Thallam, S. Wallis, L. Zhe, K.D. Cole, X33B50G(x5)T5, slab body with piecewise-constant-in-time convection at x=0 and homogeneous convection at x=1, volumetric heating that is piecewise-in-space and constant-in-time, and piecewise initial condition, Exact Analytical Conduction Toolbox (2017). https://exact.unl.edu, accessed May 14, 2020
- [47] K.D. Cole, X33B00Y33B00Z33B00Tx5y5z5, Parallelepiped with homogeneous convection boundary conditions and piecewise initial condition, Exact Analytical Conduction Toolbox (2018). http://exact.unl.edu, accessed October 2020
- [48] J.V. Beck, Sequential methods in parameter estimation, in: K.A. Woodbury (Ed.), Inverse Engineering Handbook, CRC Press, New York, 2003.
- [49] R. Yavari, A. Riensche, E. Tekerek, L. Jacquemetton, H. Halliday, M. Vandever, A. Tenequer, V. Perumal, A. Kontsos, Z. Smoqi, K.D. Cole, P.K. Rao, Digitally twinned additive manufacturing: real-time detection of flaws in laser powder bed fusion by combining thermal simulations with in-situ meltpool sensor data, Materials and Design 211 (2021) 110167, doi:10.1016/j.matdes.2021.
- [50] L. Wang, F. Bobaru, Connections between the meshfree peridynamics discretization and graph laplacian for transient diffusion problems, Journal of Peridynamics and Nonlocal Modeling (2021), doi:10.1007/s42102-021-00053-2.
- [51] R. Yavari, R.J. Williams, A. Riensche, P.A. Hooper, K.D. Cole, L. Jacquemetton, H.S. Halliday, P.K. Rao, Thermal modeling in metal additive manufacturing using graph theory – application to laser powder bed fusion of a large volume impeller, Addit. Manuf. 41 (2021) 101956, doi:10.1016/j.addma.2021.101956.